



HAL
open science

Coupling of turbulence wall models and immersed boundaries on Cartesian grids

Shang-Gui Cai, Johan Degryny, Jean-François Boussuge, Pierre Sagaut

► **To cite this version:**

Shang-Gui Cai, Johan Degryny, Jean-François Boussuge, Pierre Sagaut. Coupling of turbulence wall models and immersed boundaries on Cartesian grids. *Journal of Computational Physics*, 2021, 429, pp.109995. 10.1016/j.jcp.2020.109995 . hal-03597064

HAL Id: hal-03597064

<https://hal.science/hal-03597064>

Submitted on 4 Mar 2022

HAL is a multi-disciplinary open access archive for the deposit and dissemination of scientific research documents, whether they are published or not. The documents may come from teaching and research institutions in France or abroad, or from public or private research centers.

L'archive ouverte pluridisciplinaire **HAL**, est destinée au dépôt et à la diffusion de documents scientifiques de niveau recherche, publiés ou non, émanant des établissements d'enseignement et de recherche français ou étrangers, des laboratoires publics ou privés.

Coupling of turbulence wall models and immersed boundaries on Cartesian grids

Shang-Gui Cai^{a,*}, Johan Degrygné^b, Jean-François Boussuge^b, Pierre Sagaut^a

^a Aix Marseille Univ, CNRS, Centrale Marseille, M2P2 UMR 7340, Marseille 13451, France

^b CERFACS, Toulouse, France

ARTICLE INFO

Article history:

Received 26 February 2020

Received in revised form 24 September 2020

Accepted 6 November 2020

Available online 12 November 2020

Keywords:

Immersed boundary method

Wall model

High Reynolds number

Reynolds-averaged Navier–Stokes equations

ABSTRACT

An improved coupling of immersed boundary method and turbulence wall models on Cartesian grids is proposed, for producing smooth wall surface pressure and skin friction at high Reynolds numbers. Spurious oscillations are frequently observed on these quantities with most immersed boundary wall modeling methods, especially for the skin friction which is found to be very sensitive to the solid surface's position and orientation against the Cartesian grids. The problem originates from the irregularity of the wall distance on the stair-step grid boundaries where the immersed boundary conditions are applied. To reduce this directional error, several modifications are presented to enhance the near wall solution. First, the commonly used interpolation for the flow velocity is replaced by one for the friction velocity, which has much less variation near wall. The concept of using a fictitious point to retrieve flow fields in the wall normal direction is abandoned and the interpolation is performed in the wall parallel plane with existing fluid points. Secondly, the velocity gradients at the approximated boundary are computed with advanced schemes and the normal gradient of the tangential velocity is reconstructed from the wall laws. To further protect the near wall solution, the normal velocity gradient and the working viscosity from the Spalart-Allmaras turbulence model are enforced by their theoretical solutions in the interior fluid close to the wall. Additionally, various post-processing algorithms for reconstructing wall surface quantities and force integrations are investigated. Other related factors are also discussed for their effects on the results. The validity of present method has been demonstrated through numerical benchmark tests on a flat plate at zero pressure gradient, both aligned and inclined with respect to the grid, as well as aerodynamic cases of NACA 23012 airfoil and NASA trap wing.

1. Introduction

The immersed boundary method (IBM) has become an extremely powerful tool in a wide range of academic and industrial flow applications dealing with complex, deforming or moving geometries [1–3]. Owing to its non-body conforming grid feature, it enables flow simulations on a very simple stationary computational grid, usually the Cartesian grid, that encompasses the solid bodies. The IBM hence also goes under other names, including the Cartesian grid method [4–6], the immersed interface method [7], the embedded boundary method [8], the fictitious domain method [9], etc. It considerably

* Corresponding author.

E-mail address: shanggui.cai@univ-amu.fr (S.-G. Cai).

releases the heavy burden of building suitable body-fitted grids required by traditional methods and hence greatly accelerates the simulation processes. It also enhances the stability and improves the accuracy within the fluid by the quality of orthogonal grids. Furthermore, it facilitates the implementation of simple and highly efficient numerical methods, such as the Cartesian Navier-Stokes finite difference method and the Lattice Boltzmann method (LBM) that are anticipated to be the first CFD codes in achieving industrial large eddy simulation [10].

The flexibility of grid generation comes at a price of the imposition of boundary conditions on locations other than the physical surfaces, referred as the immersed boundary condition (IBC). To implement this condition one class of IBMs uses an extra forcing function that is determined from constitutional laws [11–15], artificial spring [16], feedback control [17], penalization [18], time discrete solution [19,20] or Lagrange multiplier [9,21–23]. The flow equations are solved over the entire domain, including inside the solid which is filled with fluid, where the IBC is treated as an internal condition. This requirement however limits its use at high Reynolds number as the number of grid points inside the solid region grows rapidly under isotropic refinement in IBM [2]. Additionally, the force term defined on the solid surface grid has to be distributed over a thin band of neighboring fluid nodes to take effect. This inevitably leads to a diffuse interface [3] that is less suitable for resolving the turbulent boundary layer. Another category of IBMs is to modify the computational stencil near the immersed boundaries [7,24–26]. The solution is locally reconstructed through interpolation with the IBC as an external condition. Therefore solving flow inside the solid is optional [2,1], which is well suited for high Reynolds number flows. Theoretically the locally reconstructed IBM can be expressed with an equivalent forcing term as in the diffuse interface counterpart [2], but the force is neither computed nor distributed, allowing a sharp interface representation and a better control of local accuracy. It is worth mentioning the cut-cell IBM [5,6,27] that is nearly as accurate as the body-fitted grid method. The grids in the vicinity of immersed boundaries are trimmed and reshaped to fit the geometry, hence the conservation properties are preserved. Nevertheless its extension to 3D geometries becomes quite complicated [2,3].

One prominent issue of the diffuse interface IBM and the locally reconstructed sharp interface IBM is their inability to extract smoothly varying surface quantities, such as the pressure and the skin friction, especially at high Reynolds number. In the former group, the discretization is treated in a uniform manner throughout the computational domain and the accuracy is controlled by the kernel function applied at the immersed boundaries, e.g. the smoothed delta function [12]. The spurious oscillations can be effectively reduced with sufficiently smoothed delta functions [28,29]. In the latter category, the discrete operator is modified locally and the immersed surfaces are approximated by the stair-step grid boundaries. The spatial approximation is sometimes ill-conditioned at these approximated boundaries and eventually brings in numerical oscillations. The boundary point for IBC can be defined either on the fluid side like the direct forcing IBM [30,31], or on the solid side as the ghost-cell IBM [24,25]. When a fluid point is too close to the physical surface, the interpolation/extrapolation formula becomes less accurate and may be ill-conditioned in the ghost-cell method. Huang et al. [8] suggested that the approximated boundary should not cross the physical surface to avoid this ill-conditioning. The rapid change of the wall distance of the stair-step grid boundaries induces significant gradient variations along the immersed surfaces and consequently causes the skin friction to be very sensitive to body's position and orientation. Considering the fact the geometrical conservation law is not included in the interpolation for IBC, enforcing mass conservation across the immersed boundaries can be useful in reducing these spurious wiggles [32]. Furthermore the interpolation order should be adapted to each flow problem. The commonly used linear interpolation for low Reynolds number flows is apparently not adequate at large Reynolds numbers. It is recommended to decompose the velocity into tangential and normal components and perform the interpolation separately with different levels of approximation [33–35].

At sufficiently high Reynolds numbers, wall functions are generally used to prevent the use of a huge number of nodes to capture the inner region of the turbulent boundary layer, especially in the context of IBM where grids are equally refined in all directions. The coupling of turbulent wall functions and immersed boundaries raises an additional challenge. This is due to the fact that the near wall grid resolution in the wall function approach would be too coarse to correctly interpolate variables that exhibit rapid changes in the wall normal direction and to accurately compute their gradients. Furthermore, the tangential velocity boundary condition has been changed from the no-slip boundary condition (Dirichlet type) to the stress boundary condition (Neumann type), for which accurate computation of the gradients becomes crucial. Although smoothed surface quantities have been reported with the cut-cell based immersed boundary wall modeling [36,37], the extension to 3D complicated geometries is not straightforward. The majority of immersed boundary wall modelings relies on the local reconstruction approach [38,26,39,34,40–42]. A fictitious/reference/reflecting point is often defined in the wall normal direction at a given distance where the flow field (e.g. velocity and density) is interpolated. The wall function is used to compute the friction velocity (or equivalently the wall shear stress) which is then applied to the approximated boundary. As a matter of fact, it is difficult to capture the highly non-linear velocity profile in the numerical discretization with the coarse near wall grids used with wall functions. Consequently the mass conservation problem could be significant, yielding large spurious oscillations near immersed boundaries that are gradually dissipated away from the wall. Capizzano [43] proposed a slip boundary condition by linearizing the velocity profile from the reference point down to the wall, such that the mass flux can be conserved with a second order accurate Navier-Stokes solver. Tamaki et al. [44] extended this idea to the Spalart-Allmaras turbulence model with an additional modification of the eddy viscosity (assumed to be constant below the reference point in compliance with the linear velocity profile), to further maintain the balance of the shear stress in the turbulent boundary layer. Nevertheless model equations are violated for a numerical purpose.

Several key physical and numerical elements must be coupled to obtain an accurate and efficient boundary condition in the addressed framework, among which: the physical wall model, the computation of the wall-normal gradients, and the

use of these computed gradients in the discretized wall model. The present work is devoted to a rigorous analysis of the influence of each element, and to the comparison of different variants for each element. At last, we will show that smooth results can be obtained with correct physical wall laws by enhancing near wall solutions, with special emphasis on the velocity interpolation, the gradient computation and the eddy viscosity distribution.

This paper is organized as follows. In Section 2 the general mathematical turbulent flow models with the wall function are presented. In the next section existing immersed boundary wall modeling techniques are discussed and new modifications are proposed. Numerical validations of the proposed method are provided in Section 4 considering i) the turbulent boundary layer over a flat plate at zero pressure gradient both with a grid-aligned wall and an inclined wall, ii) the turbulent flow around a NACA 23012 airfoil and iii) the turbulent flow past a three dimensional NASA trap wing. Finally conclusions are drawn in Section 5.

2. Mathematical models and methodology

2.1. Mean flow model

The following compressible Favre-Averaged Navier-Stokes equations are used to compute steady-state mean-flow solutions

$$\frac{\partial \rho}{\partial t} + \frac{\partial \rho u_j}{\partial x_j} = 0, \quad (1)$$

$$\frac{\partial \rho u_i}{\partial t} + \frac{\partial \rho u_i u_j}{\partial x_j} = -\frac{\partial p}{\partial x_i} + \frac{\partial \tau_{ij}}{\partial x_j}, \quad (2)$$

where u_i , ρ and p are the mean velocity components, the density and the pressure respectively. The total shear stress tensor τ_{ij} consists of the viscous stress part and the Reynolds stress part

$$\tau_{ij} = \tau_{ij}^v + \tau_{ij}^R, \quad (3)$$

the latter being to be modeled via a turbulence model. For Newtonian fluids with the Stokes' hypothesis, the viscous stress is related to the rate of strain

$$\tau_{ij}^v = 2\mu \left(S_{ij} - \frac{1}{3} \frac{\partial u_k}{\partial x_k} \delta_{ij} \right), \quad (4)$$

where μ is molecular dynamic viscosity and the rate of strain tensor is given by

$$S_{ij} = \frac{1}{2} \left(\frac{\partial u_i}{\partial x_j} + \frac{\partial u_j}{\partial x_i} \right). \quad (5)$$

Using the eddy-viscosity approximation, the Reynolds stress is modeled by

$$\tau_{ij}^R = 2\mu_t \left(S_{ij} - \frac{1}{3} \frac{\partial u_k}{\partial x_k} \delta_{ij} \right) - \frac{2}{3} \rho k \delta_{ij}, \quad (6)$$

where μ_t denotes the eddy viscosity.

In the present work, the above equations are not directly solved but instead approximated by the lattice Boltzmann equation (LBE) for weakly compressible isothermal flows equipped with the following equation of state (see [45–47]), namely

$$p = \rho c_s^2, \quad (7)$$

where c_s is the speed of sound. In the low Mach number limit, the lattice Boltzmann method (LBM) used to solve the LBE actually acts as an artificial compressibility method for weakly compressible low-Mach RANS equations with a time marching algorithm to reach the steady state. In this case the total shear stress can be approximated as

$$\tau_{ij} = 2(\mu + \mu_t) S_{ij}, \quad (8)$$

where the turbulence kinetic energy in equation (6) is generally ignored in the context of the Spalart-Allmaras (SA) turbulence model that will be discussed in the next section.

The standard LBM BGK collision model with a single relaxation time (LBGK model) however is not stable at high Reynolds numbers due to non-physical moments in addition to physical ones. This can be effectively handled by means of regularization [45,46], which can be viewed as a special case of the multiple relaxation time model. This regularized LBGK model is improved by the hybrid recursive regularized collision model (HRR-BGK) proposed in [47–49], in which a hyper-viscosity term is introduced for further stabilization. The amplitude of this stabilizing term is explicitly tuned using the parameter σ_v , where $\sigma_v = 1$ is associated to a null hyper-viscosity. In this work, $\sigma_v = 0.98$ is found to lead to stable simulations and has shown very little influence on the aerodynamic coefficients. The LBM is further enhanced for industrial applications by

using Octree grid refinement in the region of interest. The readers are referred to [46,47,50,48,49] for more comprehensive descriptions and validations of the flow solver.

As for the boundary conditions, the free-stream velocity is usually provided at inlet boundaries while the density is prescribed at far field outlet boundaries. On solid walls, the no-slip boundary condition is imposed to the velocity in wall-resolved simulations. A null normal gradient is assumed for the density/velocity whenever the Dirichlet boundary condition is applied to the velocity/density. Provided the macroscopic boundary conditions for ρ , u_i and the symmetric part of the velocity gradient tensor, S_{ij} , the distribution functions at boundaries are reconstructed thanks to the regularized model [51–53] consistently with the treatment in the bulk fluid. LBM being an essentially compressible flow solver, acoustic waves can be reflected back into the domain from the artificially truncated far field boundaries and deteriorate the interior solution. To minimize the spurious reflections, sponge/absorbing layers are set up in the vicinity of far field boundaries [54,53] and implemented as an external forcing function in the solver.

2.2. Turbulence model

The Spalart-Allmaras (SA) turbulence model is very attractive due to its simplicity, robustness and low computational cost, since it computes directly the eddy viscosity without calculating the turbulence time and length scales as in the two-equation models. It is also more versatile than algebraic models as it accounts for the transport and history effects.

Considering the fact that the eddy viscosity ν_t equals to $\kappa u_\tau d$ only in the logarithmic layer, with d being the wall distance, the SA turbulence model defines a new eddy viscosity, namely the working viscosity $\tilde{\nu}$, such that $\tilde{\nu} = \kappa u_\tau d$ is valid all the way down to the wall. This property is beneficial for numerical solutions, especially in the context of immersed boundary formulation, as the unknown has a linear behavior near the boundary. To this end, the damping function f_{v1} is introduced as

$$\nu_t = \tilde{\nu} f_{v1}, \quad f_{v1} = \frac{\chi^3}{\chi^3 + c_{v1}^3}, \quad \chi = \frac{\tilde{\nu}}{\nu}, \quad c_{v1} = 7.1. \quad (9)$$

The value of f_{v1} goes to 1 in the logarithmic layer hence $\nu_t = \tilde{\nu} = \kappa u_\tau d$ is preserved, while f_{v1} approaches 0 in the viscous sublayer as shown in Fig. 1.

Among numerous variants, the SA model with a f_{v3} term described in [55–58] is selected in present work. The transport equation for $\tilde{\nu}$ is

$$\frac{D\tilde{\nu}}{Dt} \equiv \frac{\partial \tilde{\nu}}{\partial t} + u_j \frac{\partial \tilde{\nu}}{\partial x_j} = c_{b1} \tilde{S} \tilde{\nu} - c_{w1} f_w \left(\frac{\tilde{\nu}}{d} \right)^2 + \frac{1}{\sigma} \left[\frac{\partial}{\partial x_j} \left((\nu + \tilde{\nu}) \frac{\partial \tilde{\nu}}{\partial x_j} \right) + c_{b2} \left(\frac{\partial \tilde{\nu}}{\partial x_j} \right)^2 \right], \quad (10)$$

where the three terms in the right-hand-side represent production, destruction and diffusion respectively. Their components are described by

$$\begin{aligned} \tilde{S} &= f_{v3} \Omega + \frac{\tilde{\nu}}{\kappa^2 d^2} f_{v2}, \quad \Omega = \sqrt{\frac{1}{2} \left(\frac{\partial u_i}{\partial x_j} - \frac{\partial u_j}{\partial x_i} \right)^2}, \\ f_{v2} &= \left(1 + \frac{\chi}{c_{v2}} \right)^{-3}, \quad f_w = g \left[\frac{1 + c_{w3}^6}{g^6 + c_{w3}^6} \right]^{1/6}, \\ g &= r + c_{w2} (r^6 - r), \quad r = \min \left[\frac{\tilde{\nu}}{\tilde{S} \kappa^2 d^2}, 10 \right], \\ f_{v3} &= \frac{(1 + \chi f_{v1})(1 - f_{v2})}{\chi}, \end{aligned} \quad (11)$$

where the damping functions are plotted in Fig. 1 and the model constants are given by

$$\begin{aligned} c_{b1} &= 0.1355, \quad \sigma = \frac{2}{3}, \quad c_{b2} = 0.622, \quad \kappa = 0.41, \\ c_{w1} &= \frac{c_{b1}}{\kappa^2} + \frac{1 + c_{b2}}{\sigma}, \quad c_{w2} = 0.3, \quad c_{w3} = 2, \quad c_{v2} = 5. \end{aligned} \quad (12)$$

The choice of the SA- f_{v3} version aims at preventing negative values in the source term. Since in the original definition of the SA turbulence model [59] where $f_{v3} = 1$ and $f_{v2} = 1 - \chi/(1 + \chi f_{v1})$, \tilde{S} might become zero or even negative as this f_{v2} function is negative for small χ near wall. This could disturb the r function in the model and cause numerical troubles especially near reattachment. It is therefore important to keep \tilde{S} positive and it is sometimes recommended to be greater than 0.3Ω [58]. To this end, \tilde{S} can be numerically clipped to a certain value. Piece-wise formulations are provided in [58] by using either a modified form of \tilde{S} for $\tilde{S} < 0.3\Omega$ or a different transport equation of $\tilde{\nu}$ for $\tilde{\nu} < 0$ (the negative

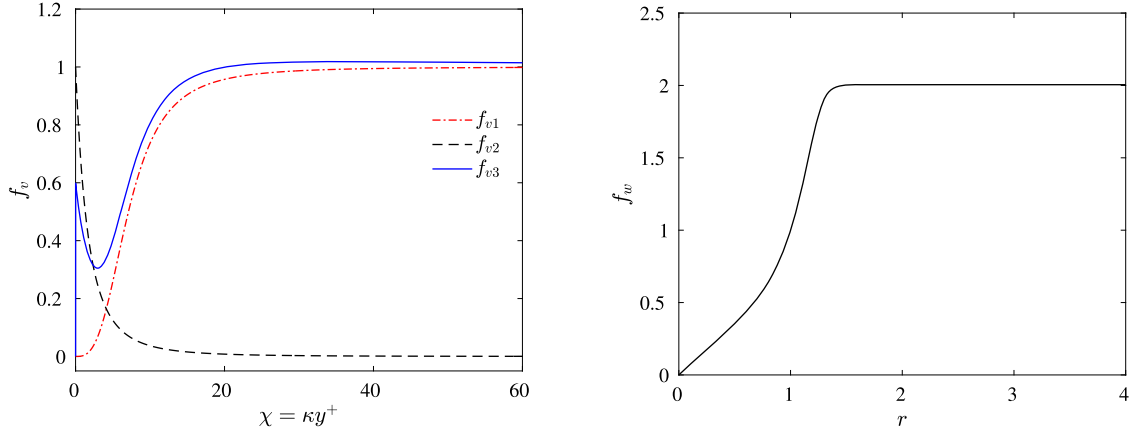


Fig. 1. Damping functions in the SA- f_{v3} turbulence model.

SA turbulence model). The SA- f_{v3} version simplifies the analysis and implementation of two distinct equations. Hence it is employed throughout this work.

In the actual numerical implementation, equation (10) is recast as follows for the non-dimensional variable $\chi = \tilde{v}/\nu$

$$\frac{D\chi}{Dt} \equiv \frac{\partial\chi}{\partial t} + u_j \frac{\partial\chi}{\partial x_j} = c_{b1} \tilde{S} \chi - c_{w1} f_w \nu \left(\frac{\chi}{d} \right)^2 + \frac{\nu}{\sigma} \left[(1 + \chi) \frac{\partial^2 \chi}{\partial x_j \partial x_j} + (1 + c_{b2}) \left(\frac{\partial \chi}{\partial x_j} \right)^2 \right]. \quad (13)$$

In the wall layer the eddy viscosity transport equation reaches an equilibrium state $D\chi/Dt = 0$ [59,60], hence it can be further simplified and non-dimensionalized to

$$c_{b1} \tilde{S}^+ \chi - c_{w1} \left(\frac{\chi}{y^+} \right)^2 + \frac{1}{\sigma} \left[(1 + \chi) \frac{\partial^2 \chi}{\partial y^+ \partial y^+} + (1 + c_{b2}) \left(\frac{\partial \chi}{\partial y^+} \right)^2 \right] = 0, \quad (14)$$

with

$$\tilde{S}^+ = \frac{\nu}{u_\tau^2} \tilde{S} = f_{v3} \frac{du^+}{dy^+} + \frac{\chi}{(\kappa y^+)^2} f_{v2}, \quad (15)$$

where we have $\Omega = du/dy$ in the near wall region and $y^+ = u_\tau d/\nu$. Both r and f_w are designed to approach 1 in the wall layer and to decrease away from the wall [59].

In the logarithmic layer, $du^+/dy^+ = 1/(\kappa y^+)$, $f_{v2} \rightarrow 0$ and $f_{v3} \rightarrow 1$. Therefore $\tilde{S}^+ = 1/(\kappa y^+)$ and equation (14) becomes

$$c_{b1} \left[\frac{\chi}{\kappa y^+} - \left(\frac{\chi}{\kappa y^+} \right)^2 \right] + \frac{1 + c_{b2}}{\sigma} \left[\left(\frac{\partial \chi}{\partial y^+} \right)^2 - \left(\frac{\chi}{y^+} \right)^2 \right] + \frac{1 + \chi}{\sigma} \frac{\partial^2 \chi}{(\partial y^+)^2} = 0, \quad (16)$$

which clearly shows that $\chi = \kappa y^+$ is one of its solution. In the viscous laminar sublayer, $du^+/dy^+ = 1$, $f_{v2} \rightarrow 1$. If f_{v3} is considered to be small, we can have $\tilde{S}^+ = \chi/(\kappa y^+)^2$ and equation (14) gives to

$$\frac{1 + c_{b2}}{\sigma} \left[\left(\frac{\partial \chi}{\partial y^+} \right)^2 - \left(\frac{\chi}{y^+} \right)^2 \right] + \frac{1 + \chi}{\sigma} \frac{\partial^2 \chi}{(\partial y^+)^2} = 0, \quad (17)$$

which is also satisfied by $\chi = \kappa y^+$. Therefore, the linear behavior of χ is guaranteed in the entire wall layer and we also have $\tilde{S}^+ = 1/(\kappa y^+)$.

The eddy viscosity transport equation (13) is discretized with finite-difference in space and integrated in time using the forward Euler scheme. The centered difference scheme is applied to derivatives in the right-hand-side, except that the hybrid upwind-centered scheme is used for the convection term. To ensure the positivity of turbulence viscosity, $\chi = \max\{\chi, 10^{-4}\}$ is applied whenever χ is updated [55]. At solid wall surface, the boundary condition $\chi = 0$ is used. At inlet χ is set to 3, while $3 \sim 5$ is suggested in [59,58] (equivalent to $\nu_t/\nu = 0.2 \sim 1.3$). Zero gradient boundary condition is applied at far field boundaries $\partial\chi/\partial n = 0$.

2.3. Wall model

For turbulent flows at high Reynolds number, directly solving the flow equations in the near wall region (wall-resolved simulations within the Eddy-Resolving Approach or low-Reynolds simulations for RANS) requires a huge amount of grid

points clustered in a very thin region [61], in order to capture the rapid variation of flow quantities, e.g. the velocity. Although the SA turbulence model is well adapted down to the wall, this tremendously increases the computational time and storage. For traditional body-fitted grid methods, the grid can be condensed in the wall normal direction and stretched in the wall tangential directions. This however results in high aspect ratio cells that can undermine the stability of the solver. Meanwhile, it effectively prohibits the use of Cartesian grid based solvers due to the fact that the grids have to be locally refined in all directions. This problem can be alleviated by using the wall modeled approach thanks to some empirical and universal quantities' profiles. For the flow over a flat plate at zero pressure gradient at $x - y$ plane, the RANS momentum equation parallel to wall in the quasi-parallel flow approximation simplifies to an ordinary differential equation

$$\frac{d}{dy}[(\mu + \mu_t) \frac{du}{dy}] = 0, \quad (18)$$

with x, y being the wall parallel and normal directions here respectively. Integration along the wall normal coordinate y yields

$$(\mu + \mu_t) \frac{du}{dy} = \text{const} = \rho u_\tau^2, \quad (19)$$

where u_τ is the friction velocity defined by the wall shear stress τ_w

$$u_\tau = \sqrt{\frac{\tau_w}{\rho}}. \quad (20)$$

This indicates that the total shear stress is constant in the wall normal direction and equal to the wall shear stress. It should be emphasized that in the wall modeled approach the boundary conditions at wall are now prescribed with this wall-shear stress for the tangential velocity along with the impermeability constraint for the normal velocity [60,62], instead of the usual no-slip wall boundary condition as in the wall resolved case.

Introducing the non-dimensionalization

$$u^+ = \frac{u}{u_\tau}, \quad v_t^+ = \frac{v_t}{\nu}, \quad (21)$$

the equation (19) can be expressed as

$$(1 + v_t^+) \frac{du^+}{dy^+} = 1. \quad (22)$$

In the viscous sublayer where $v_t^+ \ll 1$, the linear law is obtained

$$u^+ = f(y^+)_{\text{lam}} = y^+. \quad (23)$$

In the inertial range, v_t^+ is proportional to the wall distance

$$v_t^+ = \kappa y^+, \quad (24)$$

which is considerably larger than one. Thus equation (22) implies the logarithmic law

$$u^+ = f(y^+)_{\text{log}} = \frac{1}{\kappa} \log(y^+) + B, \quad (25)$$

where $\kappa \approx 0.41$ and $B \approx 5.0$.

In the linear law, the friction velocity can be computed directly by

$$u_\tau = \sqrt{\frac{u\nu}{y}}. \quad (26)$$

However the logarithmic law requires an iterative process to invert the wall function for computing the skin friction, where the Newton's iteration is usually applied

$$u_\tau^{\text{new}} = u_\tau - \frac{u_\tau f(y^+) - u}{f(y^+) + y^+ (df/dy^+)}, \quad (27)$$

where

$$\frac{df_{\text{log}}}{dy^+} = \frac{1}{\kappa y^+}. \quad (28)$$

There exists wall models that accounts for the existence of the buffer layer, just between the viscous sublayer and the logarithmic layer, e.g. the wall models of Reichardt [63], Musker [64] and Spalding [65]. Allmaras et al. [58] proposed an

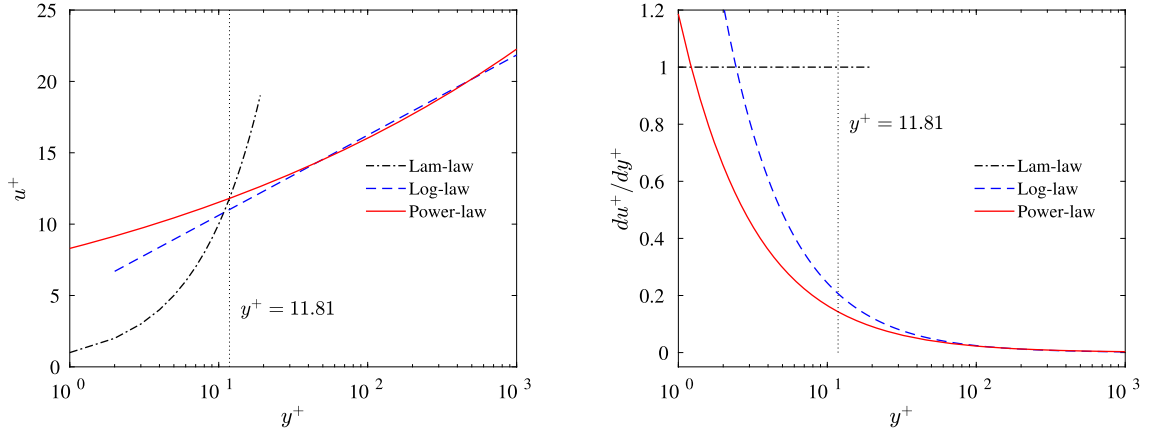


Fig. 2. Comparison of velocity profiles by different wall models.

analytical wall function that is consistent to the SA turbulence model. Knopp et al. presented a grid and flow adaptive wall model in [62]. Through adopting an appropriate damping function, the logarithmic wall model can be simply blended to the wall. Nevertheless all these models require iterations to find the friction velocity. The number of iterations is reported to be very small [44]. But this iterative process certainly slows down the whole simulation when many points are involved in the evaluation and sometimes convergence problems may occur. A tabulated solution is proposed by Kalitzin et al. [60] to circumvent this iteration, where u_τ is interpolated with a look-up table that is generated from a pre-computed fine simulation. An explicit wall model based on the power law is used in [50] for the immersed boundary wall modeling

$$u^+ = f_{\text{pow}}(y^+) = A(y^+)^B, \quad (29)$$

where $B = 1/7$. The parameter A is determined by the continuity of the velocity profile at y_{lam}^+

$$A = (y_{\text{lam}}^+)^{1-B} \approx 8.3, \quad (30)$$

where $y_{\text{lam}}^+ = 11.81$ is used in [50]. The friction velocity with power-law can be written explicitly as

$$u_\tau = u \frac{1}{1+B} A^{-\frac{1}{1+B}} y^{-\frac{B}{1+B}} \nu^{\frac{B}{1+B}}. \quad (31)$$

Fig. 2 compares the velocity profile and its derivative from different wall models. In the inertial layer, the power law approximates the logarithmic behavior and shows very little difference. But when approaching the wall, the power-law deviates from the linear behavior significantly and hence produces large errors. It is reasonable to retain the power-law for the inertial layer and use the linear law for the viscous laminar sublayer for a fully explicit wall model. To determine which profile to use, we can compare y^+ when u_τ is available. If not, we define the local Reynolds number $Re_y = yu/\nu = y^+u^+$ and compare to the critical Reynolds number $Re_c = (y_{\text{lam}}^+)^2$. The complete explicit wall model based on power law can be finally summarized as

$$u^+ = \begin{cases} f_{\text{lam}}(y^+) = y^+, & \text{if } y^+ \leq y_{\text{lam}}^+ \text{ or } Re_y \leq Re_c, \\ f_{\text{pow}}(y^+) = A(y^+)^B, & \text{if } y^+ > y_{\text{lam}}^+ \text{ or } Re_y > Re_c. \end{cases} \quad (32)$$

It should be noted that above wall model is derived under the equilibrium assumption of the turbulent boundary layer, hence it is expected to be accurate for attached flow simulations possibly with mild pressure gradient. Extended wall models taking strong adverse pressure gradients into account have been proposed, e.g. [66], but is out of the scope of the present work.

3. Immersed boundary treatment

In this section, some commonly used immersed boundary wall modeling approaches, mainly based on the local reconstruction, are first summarized and analyzed. In the following, new improvements are proposed to enhance their accuracy.

3.1. Previous immersed boundary wall modeling

The development of IBM aims at simulating flows over arbitrarily complex geometries, hence the representation of solid should be flexible enough to handle all types of geometries. Triangular surface tessellations, more precisely in the

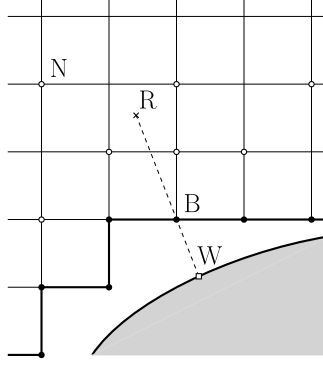


Fig. 3. Schematic of immersed boundary method. Cross: reference point; Open circle: neighbor point; Filled circle: boundary point; Open square: wall point.

stereolithography (STL) format, which are easy to generate and readily available for most CAD tools, are frequently used to represent the solid surfaces.

Once the solid surface tessellation is immersed into the fluid Cartesian grid, the fluid points inside the solid region are marked as solid points. This point tagging can be performed by ray tracing techniques [34] or simply through the dot-product of position vectors [25]. The internal treatment of the body is not relevant and does not influence the physical flow outside [1]. Solid points can be discarded for simplicity as the flow equations are no longer solved there. At high Reynolds number flows, the solid points are completely removed to save memory in [47,50].

An identification procedure is then necessary to distinguish the interior points (fully fluid) from the boundary points (non-fully fluid) as illustrated in Fig. 3. The boundary point can be easily identified in LBM as the point which has at least one link end of nearest neighbor excluded by the immersed body. Boundary conditions are now applied at the newly emerged boundary instead of the physical surface, i.e. the immersed boundary conditions.

3.1.1. Reference point wall distance

In the traditional body fitted grid method, the friction velocity or wall shear stress is computed at the first off-wall point. However, in IBM there is no guarantee that the nearby fluid point lies on the wall normal line emitted from the wall point. Therefore a fictitious point, also coined image point in [44] or reference point in [41,50] as illustrated by point R in Fig. 3, is often defined at a given distance to wall d_R to serve as the first off-wall point, where the flow quantities are interpolated for the purpose of IBC [67,38,43,26,68,44,41,50]. To ensure that all the reference points lie within the newly generated computational domain, a minimal distance would be the diagonal length of the grid nearby, i.e. $d_R \geq \sqrt{2}h$ in 2D and $d_R \geq \sqrt{3}h$ in 3D with h being the local mesh size. Furthermore, to have all fully fluid neighbor points around R in one grid layer width, the distance should be greater than twice the diagonal length of the ambient grid, namely $d_R \geq 2\sqrt{2}h$ in 2D and $d_R \geq 2\sqrt{3}h$ in 3D [44]. Nevertheless too large distances would undermine the validity of the wall law at the reference point, it should be maintained as compact as possible.

Different computations of d_R have been proposed in the literature. In [67,38,68] this distance is locally determined by the position of the boundary point and its surrounding fluid points. Péron et al. [69] recently proposed to project the reference point onto the first fluid interior cell near wall such that the reference point consists of a watertight surface mesh around the solids. Considering that the wall functions are sensitive to the location of the first off-wall point, a globally uniform distance is found favorable to the smoothness of results [26,41]. d_R is regularized by taking the overall maximum distance from the intersections of the normal line of wall points with the nearest-to-wall grid edges in [41]. Simple constant wall distances are widely accepted, e.g. $3h$ is prescribed in [44], $2.5h$ in [50] and $1.5h$ in [26].

3.1.2. Interpolation at the reference point

To obtain flow fields at the reference point, interpolation is usually performed. On pure Cartesian grid the polynomial interpolation has been extensively used [33,24,25]. The neighbor points are chosen from a regular domain, trilateral for linear polynomial basis or quadrilateral for bilinear polynomial basis in 2D for instance, relying on the grid connectivity or the boundary intersection if necessary. The interpolation coefficients are determined through a linear system. It is less frequently used on a hierarchical Cartesian grid or unstructured grid due to the grid's irregularity.

In this case a simple way is to use the linear extrapolation based on the gradient as follows

$$\phi_R = \phi_k + \mathbf{d}_k \cdot [\nabla \phi]_k, \quad \mathbf{d}_k = \mathbf{x}_R - \mathbf{x}_k, \quad (33)$$

where ϕ_R denotes generic quantities at the reference point \mathbf{x}_R . The base point can be taken from an existing fluid neighbor point, the closest point to R in [44], where the flow quantity and its gradient are available.

The inverse distance weighting (IDW) method originally proposed by Shepard [70] is used in [50,35], which can be expressed as

$$\phi_R = \sum_k \gamma_k \phi_k / q, \quad \gamma_k = \left(\frac{1}{d_k} \right)^p, \quad q = \sum_l \left(\frac{1}{d_l} \right)^p, \quad p > 0, \quad (34)$$

where p is the power of the inverse distance and $p = 2$ is generally used. d_k is the Euclidean distance between the reference point and the neighbor point, $d_k = \|\mathbf{d}_k\|$. In [67,1,24,34,71] an alternative formulation of IDW introduced by Franke [72] is employed

$$\phi_R = \sum_k \gamma_k \phi_k / q, \quad \gamma_k = \left(\frac{H - d_k}{H d_k} \right)^p, \quad q = \sum_l \left(\frac{H - d_l}{H d_l} \right)^p, \quad p > 0, \quad (35)$$

where H represents the maximum of distance d_k , which is meant to obtain a vanishing weight at the support domain boundary. The IDW is extremely efficient and very easy to compute. It also has the property of preserving local maxima and producing smooth reconstruction [72,1,24]. But it is worth noting that the IDW can exactly reproduce constant field only.

More elaborate schemes can be used of course, such as the weighted least square (WLSQ) method [43,44]. It approximates the target function with a combination of basis functions

$$\phi(\mathbf{x}) = \mathbf{p}^T \mathbf{a}, \quad (36)$$

where \mathbf{p} is the basis vector, for example in two-dimension the linear basis $\mathbf{p} = [1 \ x \ y]^T$ and the quadratic basis $\mathbf{p} = [1 \ x \ y \ x^2 \ xy \ y^2]^T$. One distinctive feature of the WLSQ interpolation is that any function appearing in the basis function can be reproduced exactly [73]. The corresponding coefficient vector \mathbf{a} is determined by minimizing the following functional

$$J = \sum_i w(\mathbf{x}_i - \mathbf{x}_R) [\phi(\mathbf{x}_i) - \phi_i]^2 = (\mathbf{P}\mathbf{a} - \boldsymbol{\phi})^T \mathbf{W}(\mathbf{P}\mathbf{a} - \boldsymbol{\phi}), \quad (37)$$

where $\phi(\mathbf{x}_i) \neq \phi_i$ for the least square approximation. $\boldsymbol{\phi} = [\phi_1, \phi_2, \dots, \phi_n]^T$ is the nodal value vector. $\mathbf{P} = [\mathbf{p}(\mathbf{x}_1), \mathbf{p}(\mathbf{x}_2), \dots, \mathbf{p}(\mathbf{x}_n)]^T$ and $\mathbf{W} = \text{diag}(w_1, w_2, \dots, w_n)$ are the extended matrices. Setting $\partial J / \partial \mathbf{a} = 0$ yields

$$\mathbf{P}^T \mathbf{W} \mathbf{P} \mathbf{a} = \mathbf{P}^T \mathbf{W} \boldsymbol{\phi}, \quad (38)$$

and the coefficient vector is computed by solving the system

$$\mathbf{a} = (\mathbf{P}^T \mathbf{W} \mathbf{P})^{-1} \mathbf{P}^T \mathbf{W} \boldsymbol{\phi}. \quad (39)$$

Finally by substituting the reference point coordinates to the definition, its value can be obtained

$$\phi_R = \phi(\mathbf{x}_R) = \mathbf{p}^T(\mathbf{x}_R) \mathbf{a} \quad (40)$$

The dimension of the matrix $\mathbf{P}^T \mathbf{W} \mathbf{P}$ is $m \times m$, with m being the number of basis. $m = 3$ for the 2D linear basis as an example. Thus its inverse is not computationally expensive. To prevent the singularity of this coefficient matrix, $n \geq m$ is required with n being the number of neighbor points. Additionally, at least one neighboring point should not be aligned with the target one along each Cartesian direction. This however will not be an issue when the interpolation is performed in the wall parallel plane as proposed in Section 3.2.1. It can be easily verified that the WLSQ degenerates to the IDW with the constant basis. Other similar interpolation schemes from the meshless methods [74] are also used in the immersed boundary interpolation, such as the moving least square (MLS) method (with different weight functions) [75], the reproducing kernel particle method (RKPM) [13,14,76], the radial basis function (RBF) [77] etc.

3.1.3. Immersed boundary conditions at boundary point

The boundary conditions are applied on the approximated boundary in the locally reconstructed IBM, where proper definitions of the IBC are required to take into account exact boundary conditions at physical surface. The density and/or pressure is generally assumed to be constant in the wall normal direction in the turbulent boundary layer for weakly compressible isothermal flows [44,50], that is to say $\partial \rho / \partial n = 0$. Thus we have

$$\rho_B = \rho_R. \quad (41)$$

Different approximations have been applied to the normal velocity v . Considering a stationary solid boundary, the following condition

$$v_B = 0, \quad (42)$$

implies a constant profile of the normal velocity distribution from the wall to the boundary point [50]. Using the linear approximation $v = a_0 + a_1 y$ leads to [44]

$$v_B = \frac{y_B}{y_R} v_R, \quad (43)$$

where the coefficients are determined by $v = 0$ at wall and $v = v_R$ at y_R , or the quadratic approximation to $v = a_0 + a_1 y + a_2 y^2$ [38,34]

$$v_B = \frac{y_B^2}{y_R^2} v_R, \quad (44)$$

where an additional condition $\partial v / \partial n = 0$ is used to find the coefficient. Nonetheless, the influence on aerodynamic coefficients with different approximations is marginal, since the normal velocity is considerably small in the turbulent boundary layer. Once the friction velocity is calculated at the reference point, it is then applied to the boundary point from the constant wall shear stress condition. The tangential velocity is obtained by the wall function as

$$u_B = u_\tau f(y_B^+), \quad y_B^+ = \frac{y_B u_\tau}{\nu}, \quad (45)$$

at the boundary point, and χ can be given by its analytical solution near wall

$$\chi_B = \kappa y_B^+. \quad (46)$$

3.1.4. Linearization of wall function

With the aforementioned settings, significant oscillations have been observed on the wall surface pressure and skin friction distributions, along with associated erroneous values of surface-integrated quantities such as the drag and lift coefficients [44,50]. As the tangential velocity is highly non-linear along the wall normal direction in the turbulent boundary layer, the numerical method would fail to capture the steep gradient when the grid resolution is not sufficient, which is the case in wall modeled simulation. Capizzano [43] and Tamaki et al. [44] proposed to linearize the velocity profile from the reference point down to the wall. Adapting this idea to the power-law based wall function (32), the linearized wall model for $y \leq y_R$ reads

$$u^+ = \begin{cases} f_{\text{lam}}(y^+) = y^+, & \text{if } y^+ \leq y_{\text{lam}}^+ \text{ or } Re_y \leq Re_c, \\ f_{\text{lin-pow}}(y^+) = A(y_R^+)^{B-1} [B y^+ + (1-B)y_R^+], & \text{if } y^+ > y_{\text{lam}}^+ \text{ or } Re_y > Re_c, \end{cases} \quad (47)$$

which changes the boundary point tangential velocity accordingly to

$$u_B = u_R - \left[\frac{\partial f}{\partial y^+} \right]_R (y_R^+ - y_B^+) u_\tau, \quad (48)$$

or equivalently

$$u_B = \begin{cases} u_R - \frac{u_\tau^2}{\nu} (y_R - y_B), & \text{if } y^+ \leq y_{\text{lam}}^+ \text{ or } Re_y \leq Re_c, \\ u_R - B \frac{u_R}{y_R} (y_R - y_B), & \text{if } y^+ > y_{\text{lam}}^+ \text{ or } Re_y > Re_c. \end{cases} \quad (49)$$

The linearized velocity profile requires a constant ν_t below the reference point in order to maintain the balance of the wall shear stress (19). To this end, the damping function f_{v1} is modified to [44]

$$f_{v1} = r_d \frac{(\chi r_d)^3}{c_{v1}^3 + (\chi r_d)^3}, \quad (50)$$

for $y < y_R$ where $r_d = y_R / y$.

With this linearization technique, smoothed pressure and skin friction wall distributions are obtained in the framework of the Navier-Stokes solver [44]. Since it essentially modifies the governing equations to suit the numerical method, the predicted drag and lift coefficients have exhibited some discrepancies compared to the reference data [44].

3.2. Improved immersed boundary wall modeling

In the following, we propose several modifications to previous immersed boundary methods, more specifically in the framework of the LBM based solver [47,50], to prevent the numerical oscillations of the wall surface stresses and to get the correct integral forces.

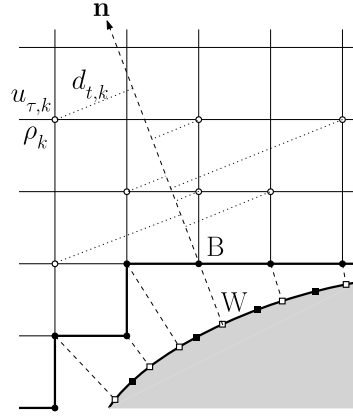


Fig. 4. Tangential interpolation for u_{τ} and ρ . Open circles, fluid interior point; Filled circles, boundary point; Open squares, projected surface points; Filled squares, existing surface grid points.

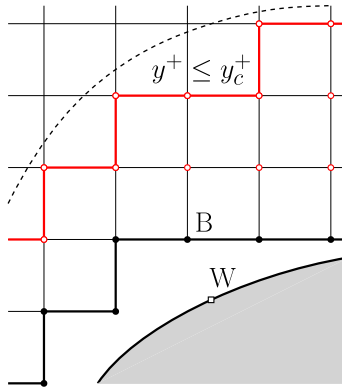


Fig. 5. Illustration of enforcing the eddy viscosity value in interior fluid points near wall, marked with red open circles. (For interpretation of the colors in the figure(s), the reader is referred to the web version of this article.)

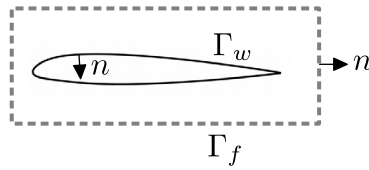


Fig. 6. Schematic of integration boundary of the far field approach and the near field approach for aerodynamic forces.

Table 1

Computational grids for the flow over a flat plate. The y^+ at the boundary point and the reference point is extracted along the plate from one of the simulations, which may slightly change among different models.

Grid	h_{\min}/L	0°		30°		45°	
		y_B^+	y_R^+	y_B^+	y_R^+	y_B^+	y_R^+
Coarse	1.4×10^{-3}	144-166	706-816	2.5-418	591-804	117-366	606-778
Medium	6.8×10^{-4}	60-90	293-440	1.2-225	290-445	28-161	287-429
Fine	3.4×10^{-4}	30-49	148-239	0.6-123	150-237	28-108	147-230

3.2.1. Tangential interpolation for u_{τ} and ρ

At high Reynolds number flows, a linear interpolation for the velocity near wall would be far from accurate. Choi et al. [35] decomposed the velocities into tangential and normal parts. A cubic function is used to construct the normal velocity and a power-law based function is applied to the tangential velocity, which is just to mimic the logarithmic behavior. However it was found that the flow pattern is closely linked to the power, which is tested from 1/9 (fully turbulent flow) or 1/7 to 1 (linear for low Reynolds number effect). Apparently, using a uniform power is not adequate for the entire region.

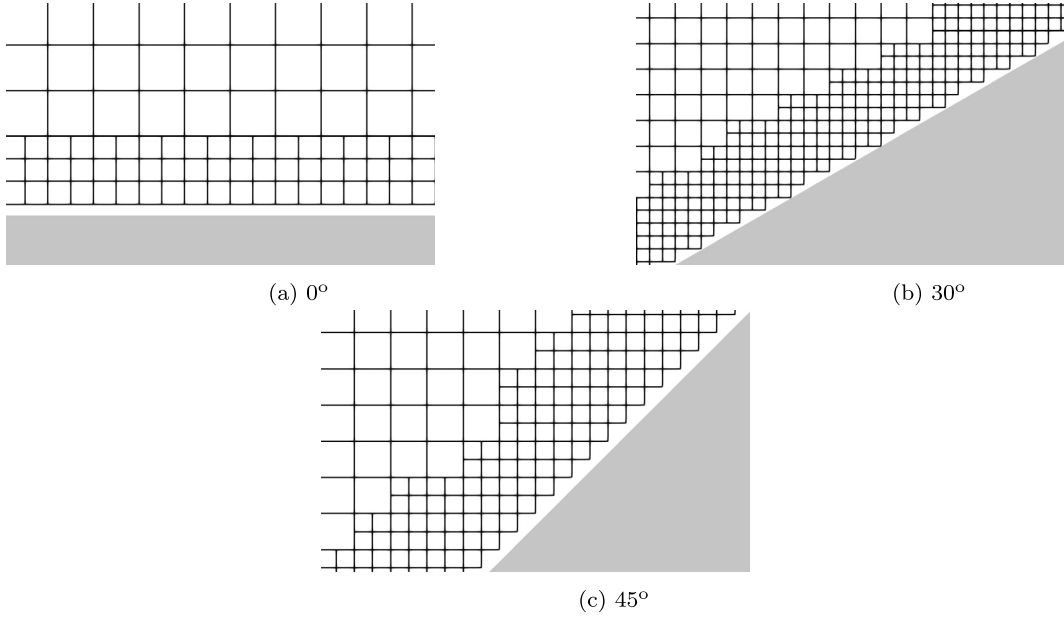


Fig. 7. Near wall grid distribution for flow over the flat plate. The coarsest grids are shown for each angle.

In present work, we propose to work on the friction velocity u_τ , which is constant in the wall normal direction. Therefore, interpolation can be performed only in the wall parallel direction. This alleviates the problem of interpolating quantities undergoing rapid changes and reduces the interpolation dimension at the same time. The procedure of this novel interpolation is performed as follows, see also Fig. 4. First we compute the tangential velocity by

$$\mathbf{u}_t = \mathbf{u} - (\mathbf{u} \cdot \mathbf{n})\mathbf{n}, \quad (51)$$

at each neighbor point, where the friction velocity is obtained by inverting the wall function. The parallel distance is calculated as

$$d_{t,k}^2 = \|\mathbf{x}_b - \mathbf{x}_k\|^2 - \|(\mathbf{x}_b - \mathbf{x}_k) \cdot \mathbf{n}\|^2 \quad (52)$$

and its inverse is used as the weight to interpolate u_τ to the boundary point. Finally the tangential velocity is recovered by the same wall law. Obviously the density at the boundary point can be interpolated with the same weight in the same manner.

It is important to note that the ambiguous reference point is no longer in use in this novel interpolation and only existing fluid points are involved. Even though the inverse of wall function is computed many more times than previously, the computational time is essentially not increased by the merit of the explicit power law based wall function.

In [50] the interpolation support domain is chosen in two grid layers using the LBM predefined lattice links from D3Q19, centered at the boundary point as shown in Fig. 3. This circumvents tedious neighbor search, but usually leaves the reference point located near the support domain boundary. In current interpolation method, the support domain becomes well defined since all the interpolations are performed in the wall parallel direction around the boundary point and consequently the interpolation dimension is reduced by one.

3.2.2. Computation of velocity gradients

The evaluation of velocity gradients is crucial in turbulence flows, especially in the immersed boundary wall modeling, as it is closely related to the wall shear stress condition near wall. This is also the main source of the spurious oscillations of the skin friction. In [47,50], the second order centered difference scheme is utilized in the core flow for high accuracy. At the boundary it simplifies to the first order one-sided finite difference scheme in the direction where one of the neighbor grid point is missing. This treatment is apparently not adequate for the turbulent boundary layer where steep gradients are present near the wall.

Higher order gradient schemes are available in the classical body-fitted grid solvers [78], such as the Green-Gauss method and the weighted least-square (WLSQ) method. The Green-Gauss formulation constructs the gradients by integrating over a control volume and expressing the gradient by the face fluxes which generally requires extra calculation if accuracy is of major concern. The WLSQ gradient scheme is unrelated to the grid topology (cell-based or vertex-based), which means that any relevant neighbor points can be selected regardless of the grid connectivity. It considers the gradient as the unknown that is solved by minimizing the error function

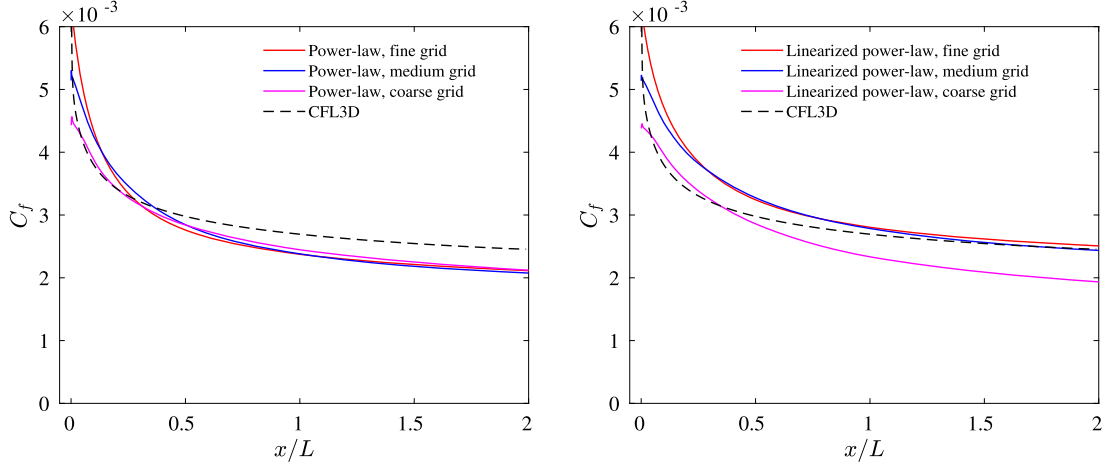


Fig. 8. Skin friction computed by the original IBM with different wall models for the flat plate simulation on the aligned grid. Left for nonlinear wall model and right for linearized wall model. (For interpretation of the colors in the figure(s), the reader is referred to the web version of this article.)

$$J = \sum_k (w_k e_k)^2 = \mathbf{e}^T \mathbf{W} \mathbf{e}, \quad (53)$$

where the weight is expressed as the usual inverse distance to give more influence to close points. Otherwise, the unweighted least-square (LSQ) is retained with the unity weight. The error term is defined by the difference between the nodal value and the linear extrapolation with the gradient

$$e_k = \phi_k - [\phi_B + \mathbf{d}_k \cdot (\nabla \phi)_B], \quad \mathbf{d}_k = \mathbf{x}_k - \mathbf{x}_B, \quad (54)$$

which can be rewritten in the vector form

$$\mathbf{e} = \phi - [\phi_B + \mathbf{D} \cdot (\nabla \phi)_B], \quad \mathbf{D} = [\mathbf{d}_1, \mathbf{d}_2, \dots, \mathbf{d}_n]^T \quad (55)$$

The weighted error is minimized when

$$\frac{\partial J}{\partial \mathbf{e}} = \mathbf{W} \mathbf{e} = 0 \quad (56)$$

which leads to

$$(\nabla \phi)_B = (\mathbf{D}^T \mathbf{W} \mathbf{D})^{-1} \mathbf{D}^T \mathbf{W} (\phi - \phi_B), \quad (57)$$

where the size of the matrix inverse $(\mathbf{D}^T \mathbf{W} \mathbf{D})^{-1}$ is proportional to the physical dimension, i.e. 2×2 for 2D and 3×3 for 3D. Hence it can be computed analytically without increasing too much computational effort. Theoretically the WLSQ gradient scheme improves the accuracy to the second order. This technique is extensively used in the Navier-Stokes based immersed boundary wall modeling of [43,44].

3.2.3. Reconstruction of the tangential velocity normal gradient

The tangential velocity exhibits steep gradients along the wall normal direction in the turbulent boundary layer as revealed by the wall function, hence it can not be accurately estimated with just a few points in the wall modeled simulation and hence needs corrections. To ensure the correct wall shear stress, the eddy viscosity is usually increased artificially at wall to compensate the under-estimation of the velocity gradient in the traditional body-fitted grid method, or equivalently through a added source term [79]. In the immersed boundary wall modeling approach of [44], the eddy viscosity is set to a constant value below the reference point that actually serves as the same purpose. In the work of [50] the eddy viscosity is recovered from the working viscosity of the SA turbulence model and the gradient is computed with the first order one-sided finite difference as

$$\left(\frac{\partial u}{\partial y} \right)_B = \frac{u_N - u_B}{y_N - y_B}, \quad (58)$$

where N denotes the neighbor point of the boundary point B in the wall normal direction (assuming the y -axis). It implies a linear variation of the flow velocity and hence is only accurate when both points reside in the viscous sublayer. It becomes erroneous when N is beyond the viscous sublayer and B is too close to wall, in this case we get $y_B \rightarrow 0$, $u_B \rightarrow 0$ and

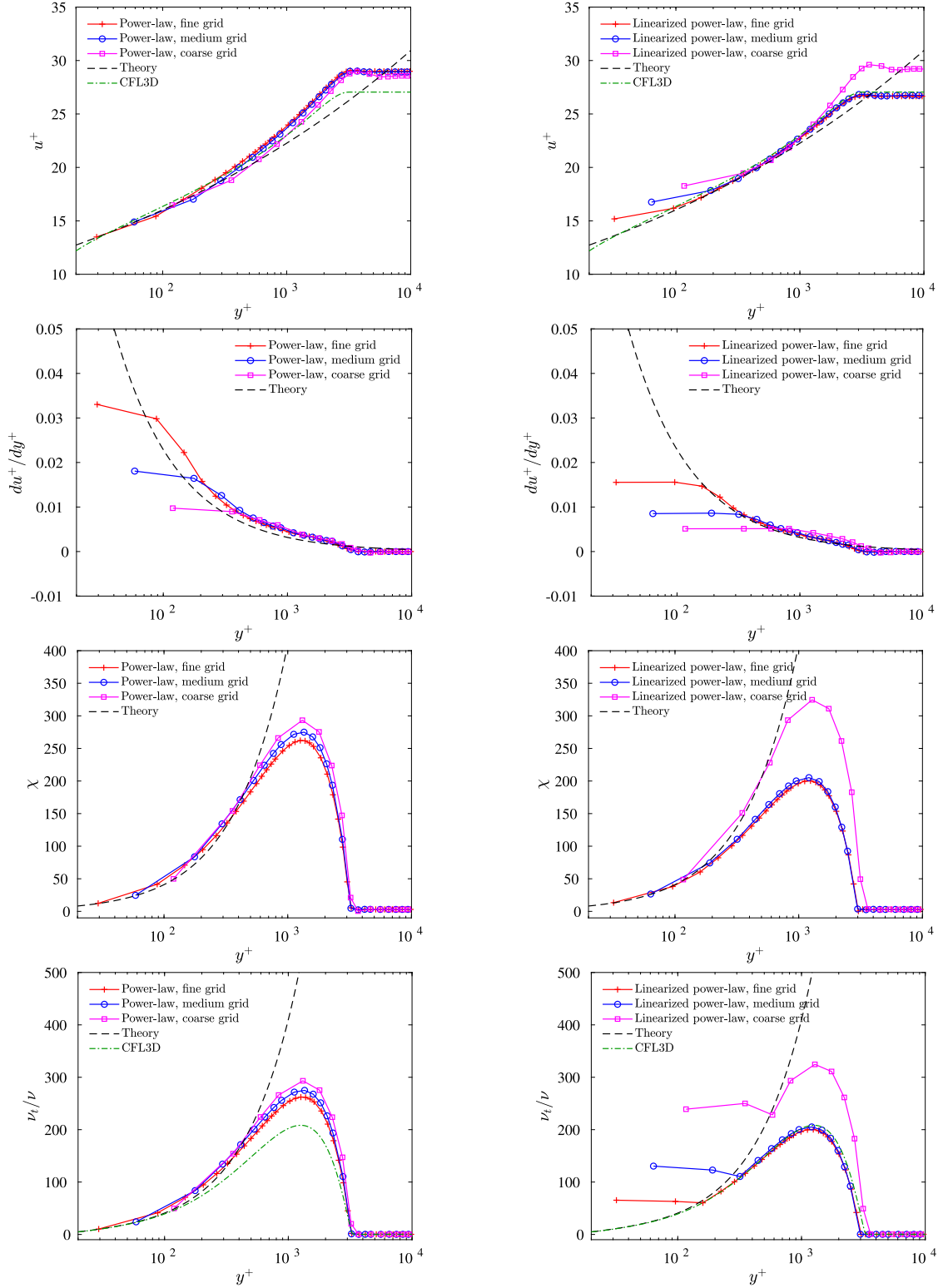


Fig. 9. Flow field profiles at $x/L = 0.97$ reproduced by the original IBM with different wall models for the flat plate simulation on the aligned grid. Left for nonlinear wall model and right for linearized wall model. (For interpretation of the colors in the figure(s), the reader is referred to the web version of this article.)

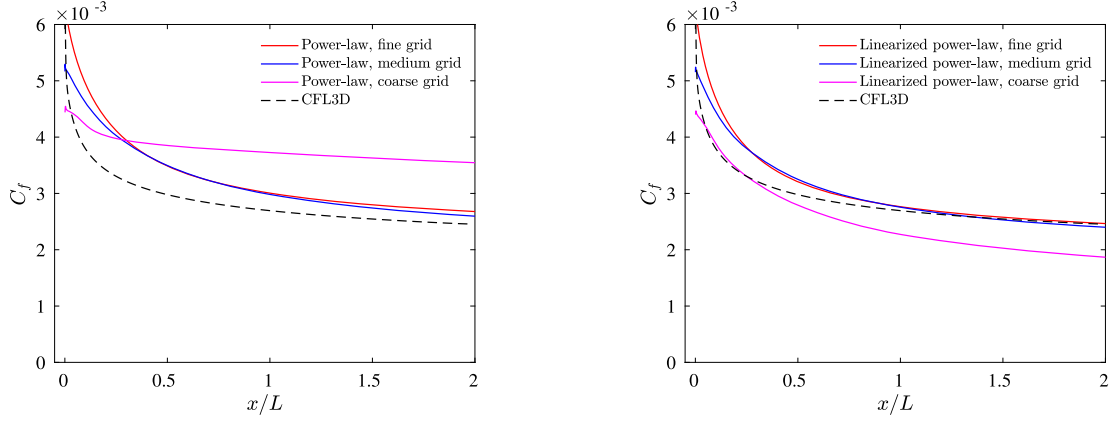


Fig. 10. Skin friction computed with the normal gradient correction for the flat plate simulation on the aligned grid. Left for nonlinear wall model and right for linearized wall model. (For interpretation of the colors in the figure(s), the reader is referred to the web version of this article.)

$$\left(\frac{\partial u}{\partial y}\right)_B \approx \frac{u_N}{y_N} \ll \left(\frac{\partial u}{\partial y}\right)_B^{\text{exact}}. \quad (59)$$

In present work we correct the velocity gradient in the turbulence boundary layer according to the wall laws with high order schemes. First the flow direction \mathbf{s} is determined by the flow velocity \mathbf{u}

$$\mathbf{s} = \frac{\mathbf{u} - (\mathbf{u} \cdot \mathbf{n})\mathbf{n}}{\|\mathbf{u} - (\mathbf{u} \cdot \mathbf{n})\mathbf{n}\|}, \quad (60)$$

where \mathbf{n} represents the outwards wall normal unit vector. The gradient tensor is transformed into the flow aligned coordinate system and its normal component is reconstructed by the third order one-sided finite difference formula

$$\left(\frac{\partial u}{\partial y}\right)_B = \frac{-11u_0 + 18u_1 - 9u_2 + 2u_3}{6h}, \quad (61)$$

where u_0 to u_3 are the tangential velocities given by the wall laws at a uniform normal spacing, starting from the boundary point into fluid interior, i.e. $u_m = u(y = y_b + mh)$. Finally the gradient tensor is transformed back to the Cartesian coordinate system. This reconstruction is performed after the computation of gradients with the WLSQ method.

3.2.4. Enforcing eddy viscosity value in the near wall cells

It has been shown previously in Section 2.2 that the non-dimensional working viscosity from the SA turbulence model has a simple near wall solution that scales linearly with the wall distance $\chi = \kappa y^+$. This linear behavior however can not be ensured in practice. First the f_{v3} term used to avoid negative source does not vanish in the viscous laminar sub-layer (see Fig. 1). Secondly, the damping function f_w varies quickly in the turbulent boundary layer with current immersed boundary wall modeling. The balance of various source terms in the eddy viscosity transport equation (13) is no longer maintained. Consequently the distribution of the eddy viscosity ν_t recovered from χ will be changed, as well as the wall shear stress.

Therefore, the working viscosity is imposed analytically on fluid interior points close to wall in order to protect the solution in the turbulent boundary layer, as well as previous normal gradient, as illustrated in Fig. 5. The criterion can be established by the geometrical wall distance $y \leq y_c$ or by the flow condition such as $y^+ \leq y_c^+$ that can be evaluated explicitly using the wall model (32) or (47), with y_c and y_c^+ being the thresholds. This treatment actually shifts the IBC location further away from the wall, similar to the near wall grid adaptation in the body-fitted grid solvers [60,62]. In current work, the flow based enforcement is recommended.

3.3. Post-processing for calculating aerodynamic coefficients

3.3.1. Surface Coefficients

Since the fluid Cartesian grid does not coincide with the surface grid in IBM, the quantities of interest (density/pressure, friction velocity, etc.) need to be reconstructed over the body surfaces, in order to compute the non-dimensional aerodynamic coefficients defined by

$$C_p = \frac{p - p_\infty}{\frac{1}{2}\rho_\infty u_\infty^2}, \quad (62)$$

$$C_f = \frac{\tau_w}{\frac{1}{2}\rho_\infty u_\infty^2} = \frac{\rho u_\tau^2}{\frac{1}{2}\rho_\infty u_\infty^2}, \quad (63)$$

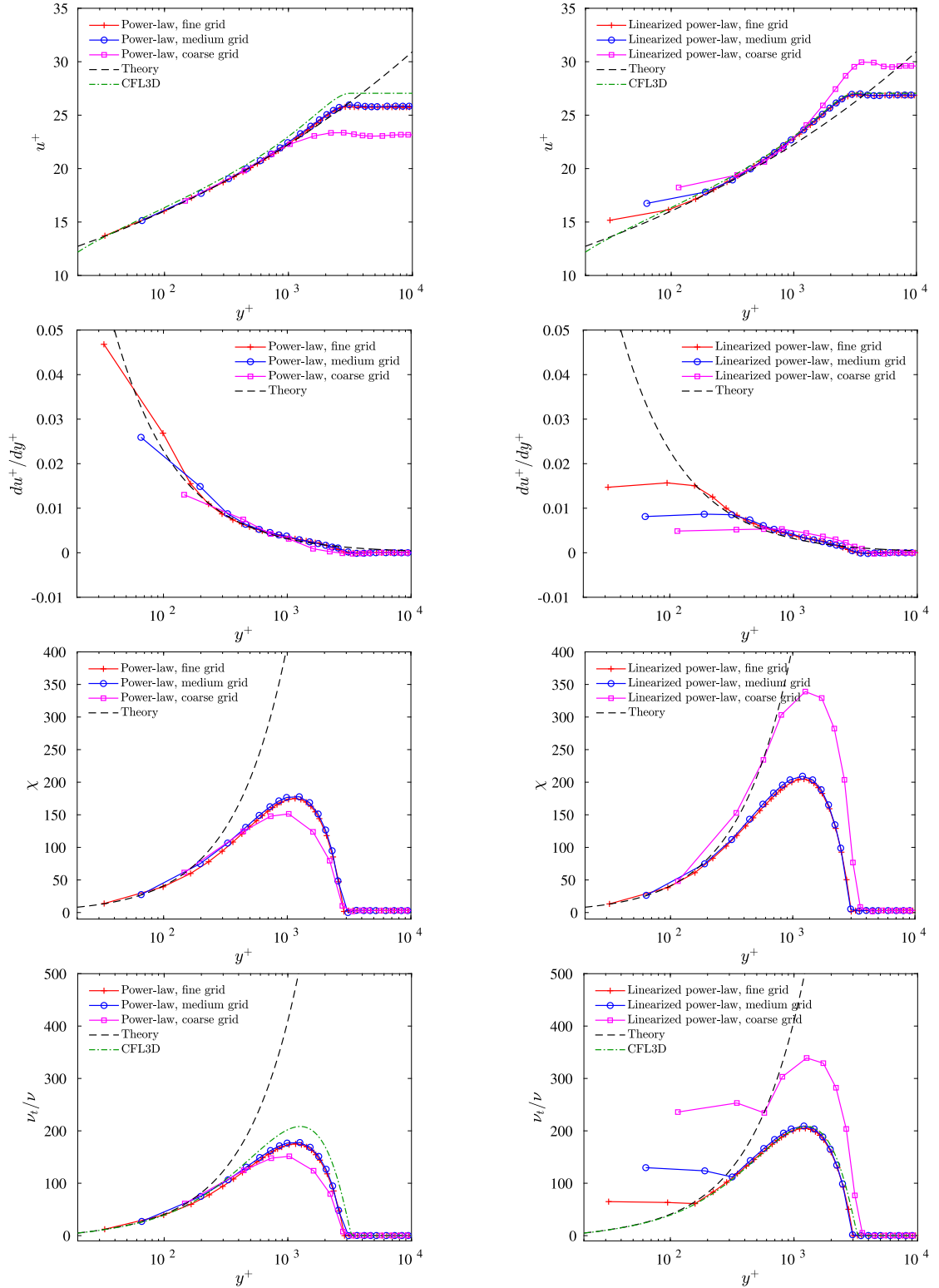


Fig. 11. Flow field profiles at $x/L = 0.97$ reproduced with the normal gradient correction for the flat plate simulation on the aligned grid. Left for nonlinear wall model and right for linearized wall model. (For interpretation of the colors in the figure(s), the reader is referred to the web version of this article.)

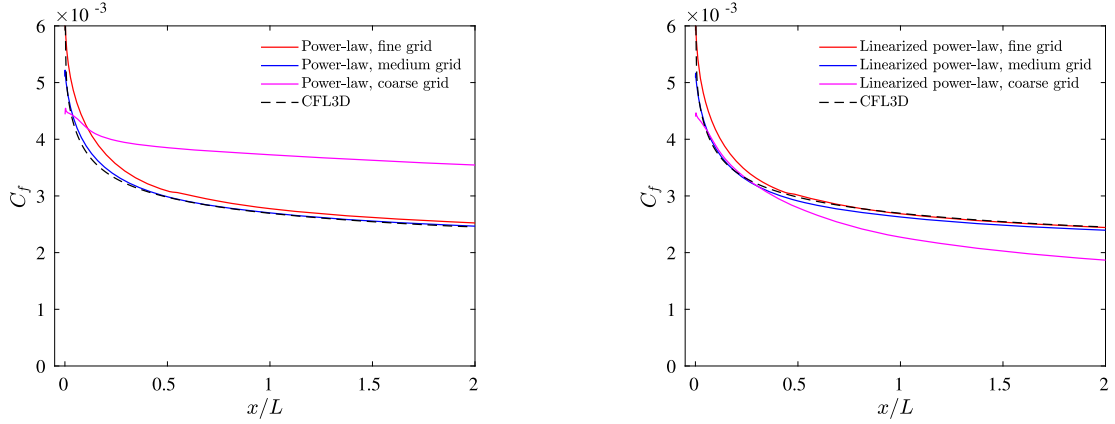


Fig. 12. Skin friction computed with the normal gradient correction and the near wall field enforcement ($y_c^+ = 300$) for the flat plate simulation on the aligned grid. Left for nonlinear wall model and right for linearized wall model. (For interpretation of the colors in the figure(s), the reader is referred to the web version of this article.)

where ρ_∞ and u_∞ are the reference density and velocity respectively. Note that in aerodynamic applications the pressure coefficient is usually presented with a negative sign in the figure results.

In [50] the inverse distance weighting algorithm is applied directly to the surface grid point using nearby fluid boundary points. Physical boundary conditions are used during the reconstruction in [44]. Two reference points are set up to extrapolate the pressure quadratically in the wall normal direction and the density is recovered through the Crocco-Busemann relationship. The friction velocity is computed from the regular reference point with the wall law.

To account for correct boundary conditions in present work, the friction velocity and the density are interpolated in the wall parallel plane to the surface grid point, as done previously for the IBC on the boundary point. Alternatively, one can project these quantities from the boundary points onto the wall surface due to their null gradient normal to the wall (see Fig. 4). The difference with the previous results is however found to be small as shown in Section 4.

3.3.2. Global Coefficients

For steady flows the integral of the momentum equation implies that

$$\int_{\partial\Omega} (-\rho u_i u_j - p \delta_{ij} + \tau_{ij}) n_j dS = 0 \quad (64)$$

where the divergence theorem is used. By decomposing the integration boundary $\partial\Omega = \Gamma_w \cup \Gamma_f$, the aerodynamic forces F_i on the body can be integrated in two distinct ways, namely the near field approach and the far field approach [80,81]

$$\begin{aligned} F_i &= \int_{\Gamma_w} (p \delta_{ij} - \tau_{ij}) n_j dS && \text{(Near field approach)} \\ &= - \int_{\Gamma_f} (\rho u_i u_j + p \delta_{ij} - \tau_{ij}) n_j dS && \text{(Far field approach)} \end{aligned} \quad (65)$$

In the near field approach, the integration is performed along the body surface Γ_w with the reconstructed pressure and wall shear stresses, where the non-penetration condition at wall is assumed. In the far field approach the forces are evaluated from the fluid side with a surrounding domain Γ_f that encompasses the object. In the work of Tamaki et al. [82] the integration domain is selected to be the staircase boundary of the approximated solid wall. In the present work, we perform the integration over a rectangular box close to the solid as also used in [50], see Fig. 6. Finally the drag and lift coefficients are defined as

$$C_d = \frac{F_d}{\frac{1}{2} \rho u_\infty^2 A_{\text{ref}}}, \quad C_l = \frac{F_l}{\frac{1}{2} \rho u_\infty^2 A_{\text{ref}}}, \quad (66)$$

where A_{ref} represents the reference area. F_d and F_l are the forces applied in the flow direction and the perpendicular direction respectively.

4. Numerical results

To check the accuracy of the proposed method and the influence of each technical ingredient on the final results, two-dimensional numerical experiments are carried out. Since the LBM based flow solver is defined in three dimensions (with

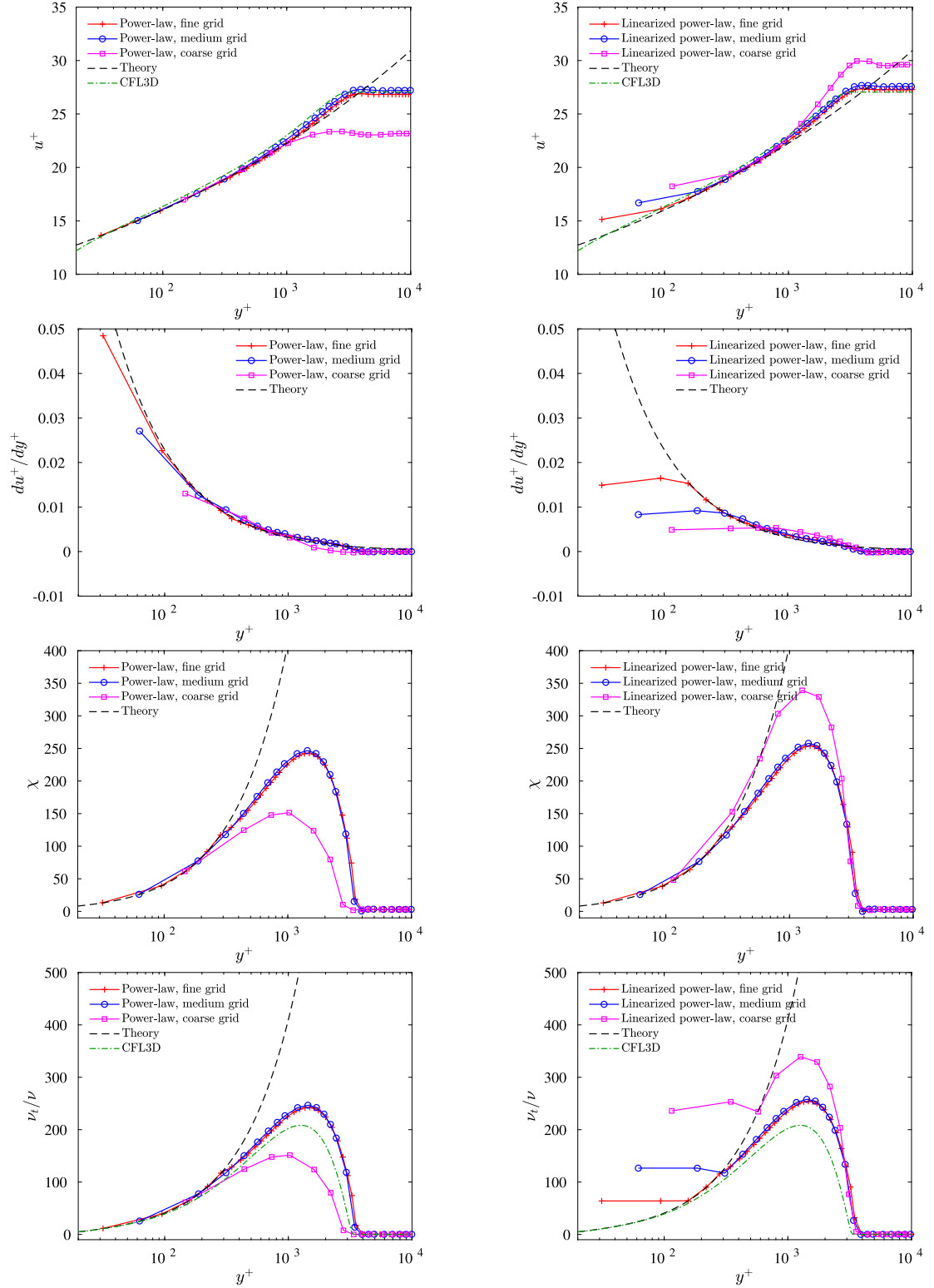


Fig. 13. Flow field profiles at $x/L = 0.97$ reproduced with the normal gradient correction and the near wall field enforcement ($y_c^+ = 300$) for the flat plate simulation on the aligned grid. Left for nonlinear wall model and right for linearized wall model. (For interpretation of the colors in the figure(s), the reader is referred to the web version of this article.)

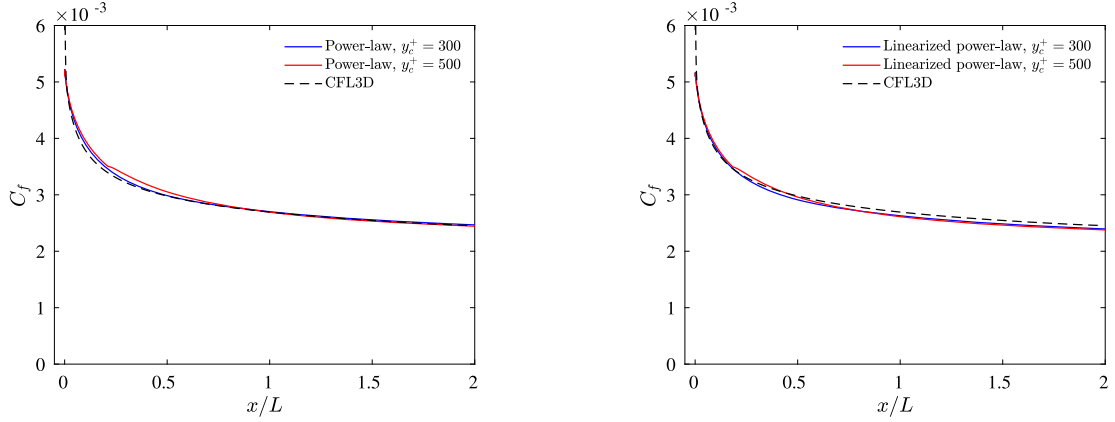


Fig. 14. Influence of the near wall field enforcement threshold for the flat plate simulation on the aligned grid. Computed on the medium grid. Left for nonlinear wall model and right for linearized wall model. (For interpretation of the colors in the figure(s), the reader is referred to the web version of this article.)

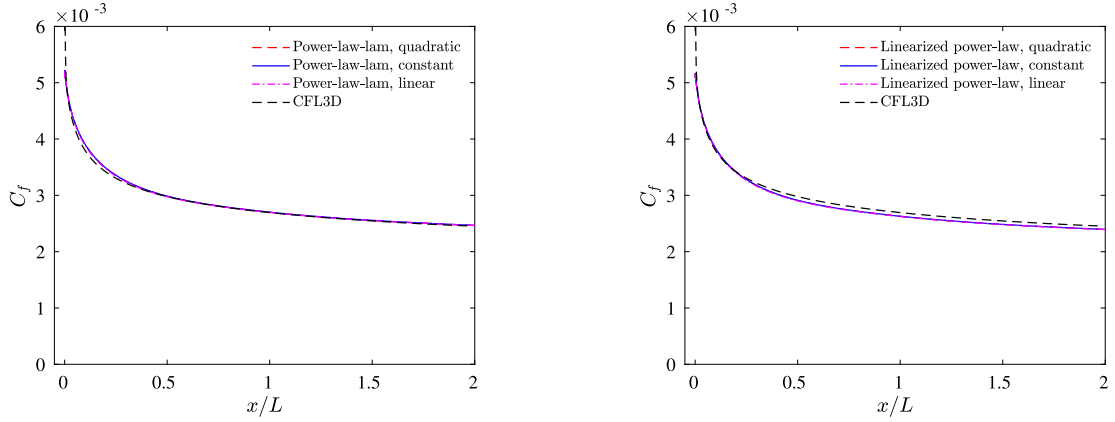


Fig. 15. Influence of the normal velocity boundary condition for the flat plate simulation on the aligned grid. Computed on the medium grid. Left for nonlinear wall model and right for linearized wall model. (For interpretation of the colors in the figure(s), the reader is referred to the web version of this article.)

the D3Q19 lattice velocity set) on the octree refined Cartesian grid, periodic boundary conditions are applied in the spanwise direction [50]. The following physical parameters are used in present study: the speed of sound $c_0 = 340$ m/s and the kinematic molecular viscosity $\nu = 1.5 \times 10^{-5}$ m²/s. The final state of the flow is assumed to be stationary and only the attached boundary layer flows are considered to guarantee an optimal accuracy of the SA turbulence model. The equation is advanced in time until convergence is reached. For better comparison, the method described in [50] will be referred as the original IBM, based on which new modifications are made towards present IBM to enhance the near wall solution. The velocity profiles used here are labeled as the non-linear wall models: the power-law (power law without viscous sub-layer) and the power-law-lam (power law with viscous sub-layer), and their linearized counterparts: the linearized power-law and the linearized power-law-lam.

4.1. Flat plate case

The two-dimensional flow over a flat plate at zero pressure gradient is considered as the first test case. This benchmark test is well documented in the NASA Turbulence Modeling Resource (TMR) website [57] with a collection of various data sets, among which the results provided by the body-fitted Navier-Stokes code CFL3D with the SA turbulence model are selected as the reference data in the present work. The Reynolds number based on the plate half-length L is $Re = 5.0 \times 10^6$ and the Mach number is $Ma = 0.2$. A small portion of free-slip wall is put before the flat plate to reduce the effect of the inlet boundary condition and the sponge layer to the zone of interest. The far field boundary is located $1.0L$ away from the flat plate. The flat plate is placed at the lower boundary of the computational domain.

In spite of this simple geometry, it turns out to be very difficult for the immersed boundary method to reproduce correctly the boundary layer. Different types of grids are constructed successively with respect to the body's relative position and orientation to the Cartesian grid. The first grid is aligned with the plate to validate the quasi body-fitted solution. Then

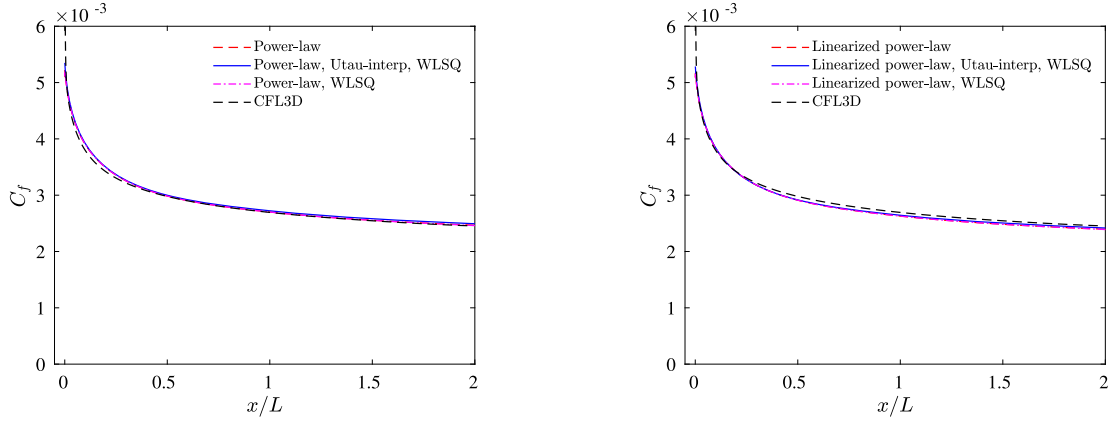


Fig. 16. Effect of u_τ interpolation and WLSQ gradient computation for the flat plate simulation on the aligned grid. Computed on the medium grid. Left for nonlinear wall model and right for linearized wall model. (For interpretation of the colors in the figure(s), the reader is referred to the web version of this article.)

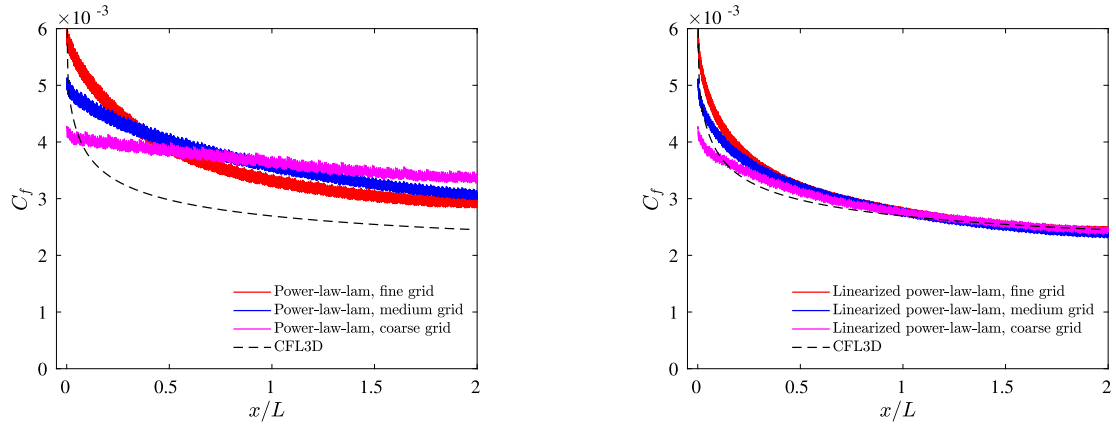


Fig. 17. Skin friction computed by the original IBM with different wall models for the flat plate simulation on the inclined grid at 30° . Left for nonlinear wall model and right for linearized wall model. (For interpretation of the colors in the figure(s), the reader is referred to the web version of this article.)

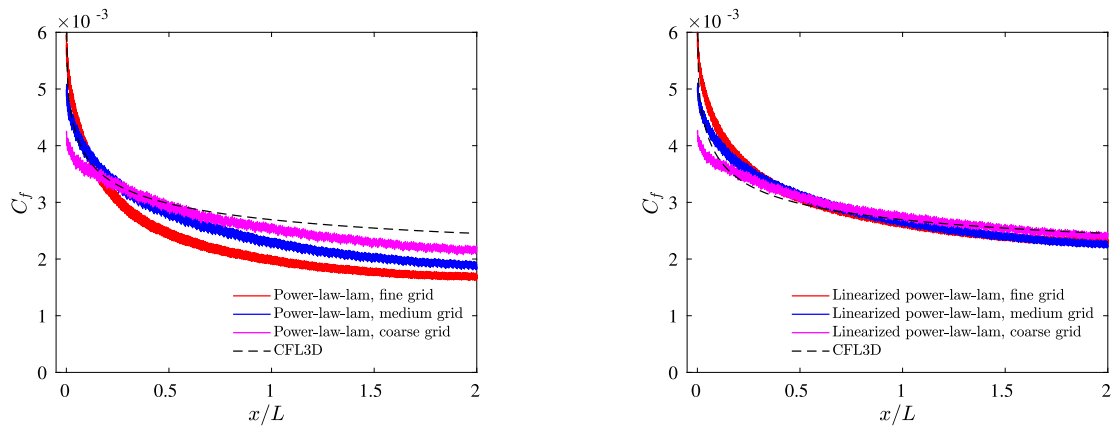


Fig. 18. Skin friction computed with the normal gradient correction for the flat plate simulation on the inclined grid at 30° . Left for nonlinear wall model and right for linearized wall model. (For interpretation of the colors in the figure(s), the reader is referred to the web version of this article.)

the grids are inclined at two different angles 30° and 45° with respect to the plate. In the inclined settings, the new boundary becomes irregular like a stair-case and its wall distance is no longer smooth along the plate, especially at the low angle 30° . Fig. 7 shows the near wall grid distributions for the aligned and inclined arrangements. Grid convergence studies are carried out on three different grid sizes, which are summarized in Table 1.

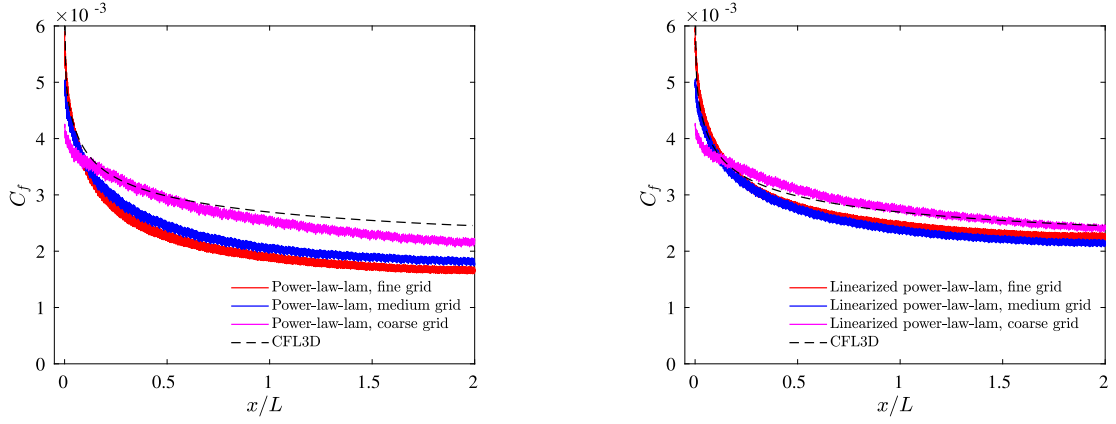


Fig. 19. Skin friction computed with the normal gradient correction and the near wall field enforcement for the flat plate simulation on the inclined grid at 30° . Left for nonlinear wall model and right for linearized wall model. (For interpretation of the colors in the figure(s), the reader is referred to the web version of this article.)

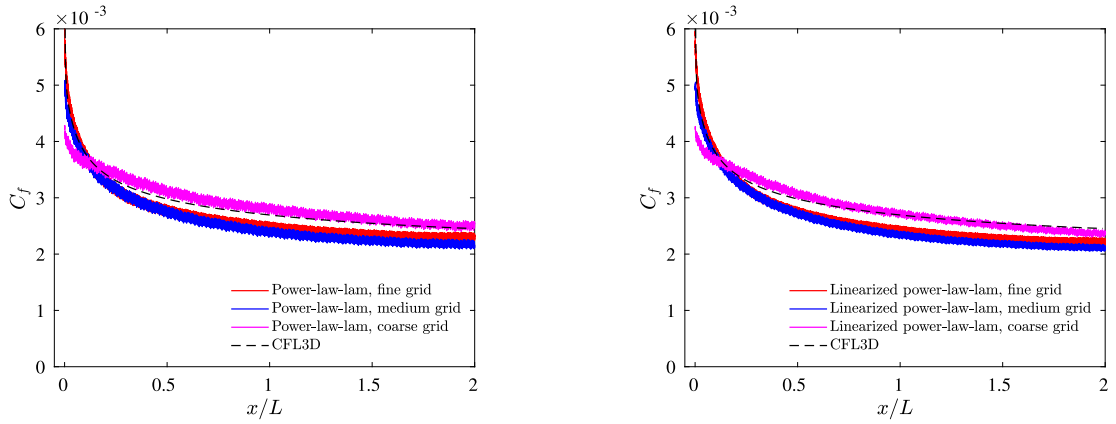


Fig. 20. Skin friction computed with the normal gradient correction, the near wall field enforcement and the WLSQ gradient method for the flat plate simulation on the inclined grid at 30° . Left for nonlinear wall model and right for linearized wall model. (For interpretation of the colors in the figure(s), the reader is referred to the web version of this article.)

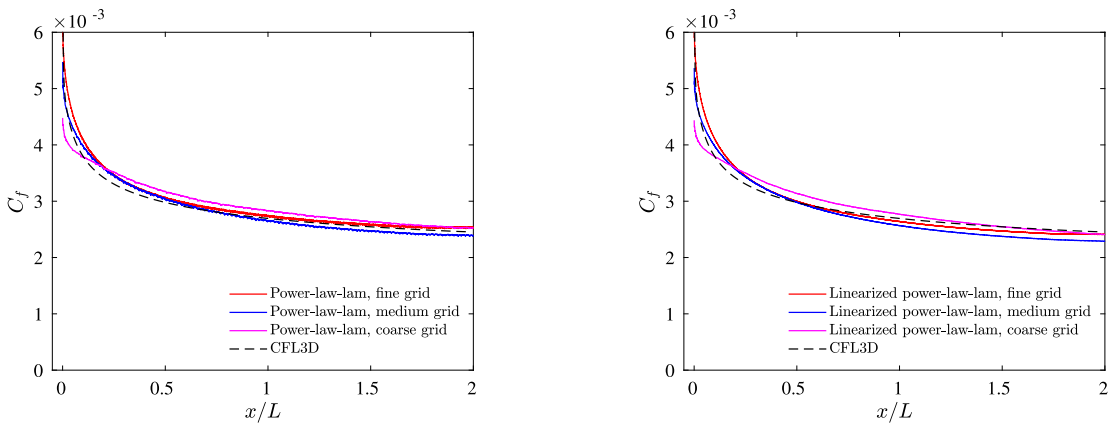


Fig. 21. Skin friction computed with the normal gradient correction, the near wall field enforcement, the WLSQ gradient method and the u_τ interpolation for the flat plate simulation on the inclined grid at 30° . Left for nonlinear wall model and right for linearized wall model. (For interpretation of the colors in the figure(s), the reader is referred to the web version of this article.)

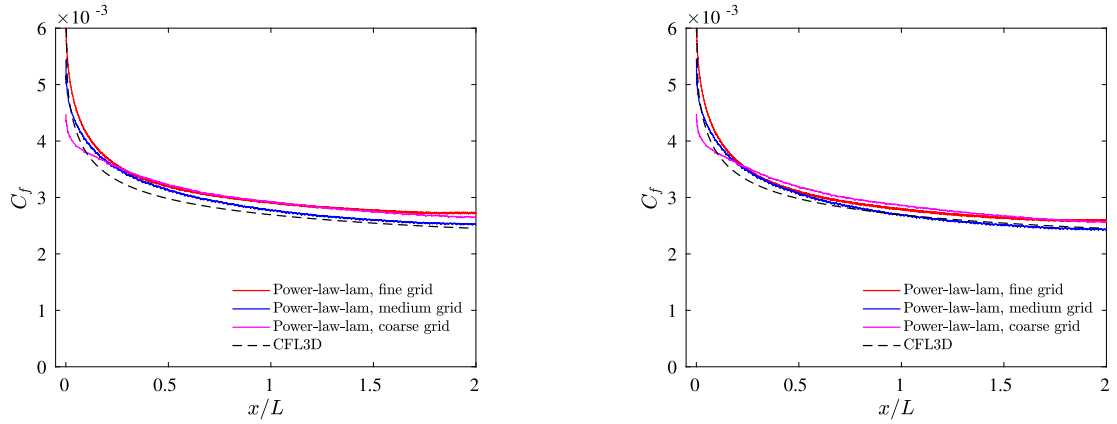


Fig. 22. Comparison of normal velocity boundary conditions for the flat plate simulation on the inclined grid at 30° . Left for linear approximation and right for quadratic approximation. (For interpretation of the color(s) in the figure(s), the reader is referred to the web version of this article.)

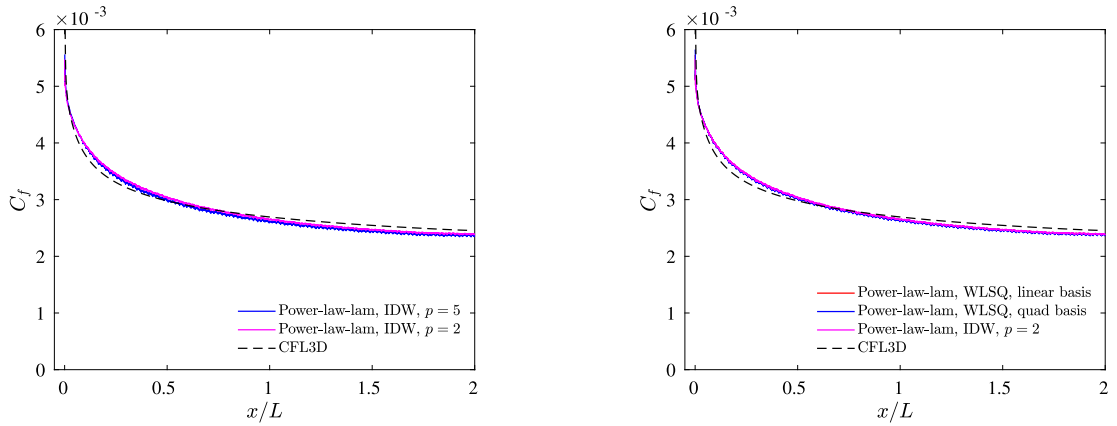


Fig. 23. Comparison of interpolation methods for the flat plate simulation on the inclined grid 30° . Computed on the medium grid. (For interpretation of the color(s) in the figure(s), the reader is referred to the web version of this article.)

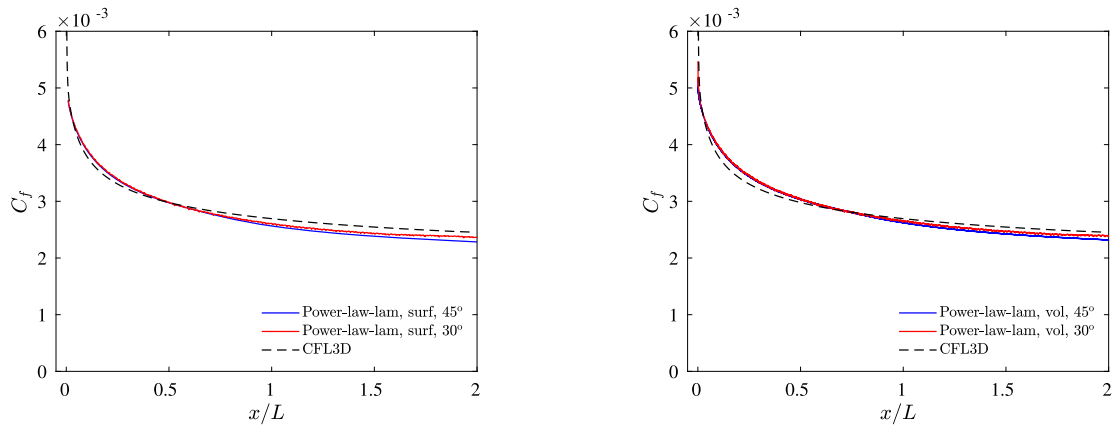


Fig. 24. Comparison of postprocessing techniques for the flat plate simulation on the inclined grid 30° and 45° . Computed on the medium grid. (For interpretation of the color(s) in the figure(s), the reader is referred to the web version of this article.)

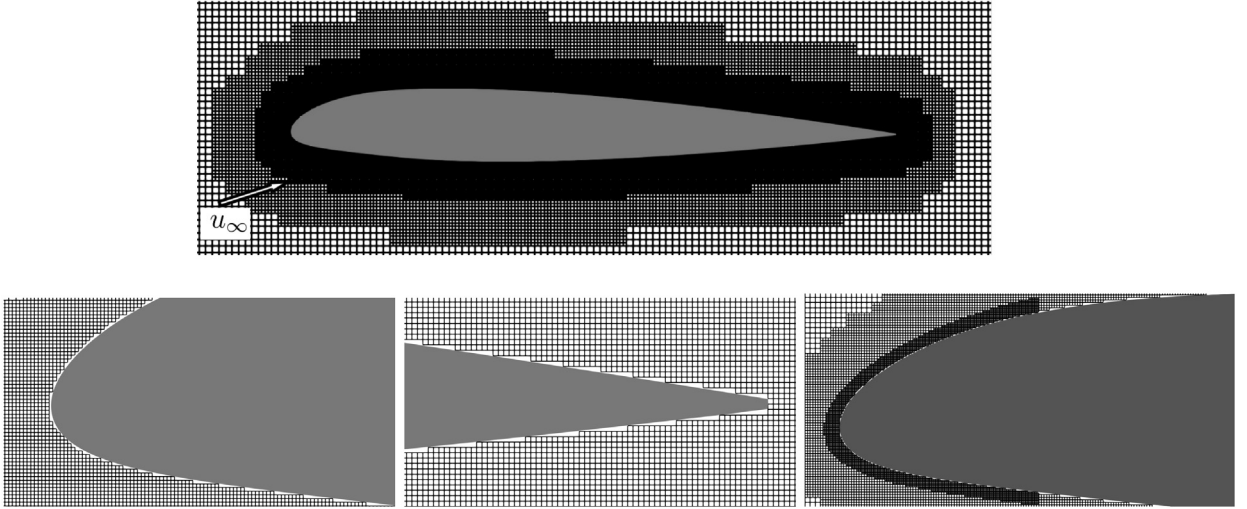


Fig. 25. Near wall grid for the NACA 23012 airfoil case. Top for the overall view; Bottom left for the leading edge; Bottom middle for the trailing edge; Bottom right for the leading edge with local refined grid.

In the aligned case, the computational domain is shifted by a distance of $0.5h_{\min}$ such that the viscous sublayer profile is not triggered near wall during grid refinements (see Table 1 for y^+). It allows minimizing the effect of the buffer layer that is absent in current power-law based wall model and to simplify the discussion of each technique proposed previously. Fig. 8 shows the skin friction along the plate calculated by the original IBM with different wall models. The smooth variation of the skin friction is expected since the wall distance is uniform when the grid is parallel to the plate. However, the obtained skin friction deviates considerably from the reference data in the non-linear wall model, which is over-estimated in the beginning of the plate and becomes under-estimated in the downstream. On the other hand, the linearized wall model gives good predictions in the downstream part of the plate but over-estimates the skin friction in the beginning of the plate under different grid resolutions.

The profiles of flow fields at $x/L = 0.97$ are shown in Fig. 9, which are extracted directly from the physical points such that no interpolation error is introduced. As the velocity gradient and the eddy viscosity are numerically set to be constant in the linearized wall model, the model equations are not fully obeyed below the reference point. Nevertheless it gives good predictions for the velocity and the eddy viscosity far away from the wall with respect to the results of CFL3D, except for the coarse grid. Using the non-linear wall model, even though the underlying model equations is respected, the numerical results are not satisfactory. The velocity and the eddy viscosity profiles converge to a higher level with respect to the CFL3D results. Moreover, the near wall velocity gradient is not well computed in the non-linear wall model, which is erroneous at the boundary point. This is not surprising since the velocity gradient is only computed with the first order one-sided finite difference scheme, which is not capable of capturing this steep gradient. This treatment of course causes no difficulties in the linearized wall model.

As a matter of fact, the computed gradient strongly affects the damping function f_w which is used to sustain the destruction of the eddy viscosity in the wall layer. Consequently the theoretical linear variation of the working viscosity near wall can hardly be maintained. It is claimed in [44] that this linear solution will not be altered by the linearization procedure with the standard SA turbulence model. However this does not hold for the SA- f_{v3} version, since the production term is changed by the modified velocity gradient and the near wall equations (16) and (17) are independent of the modification of f_{v1} . It can be verified from Fig. 9 that the working viscosity deviates from the linear solution more easily in the linearized wall model, which finally affects the distribution of the eddy viscosity and total shear stress.

To overcome the gradient error in the wall shear stress, the eddy viscosity at the wall is often modified in the traditional body fitted wall modeling, or equivalently a source term is added at the wall [79]. In the present work, the gradient itself is directly corrected using the law of the wall by equation (61). The computed skin friction is compared in Fig. 10. Correcting the normal gradient eventually increases the skin friction in the non-linear wall model. The profiles of the eddy viscosity, the tangential velocity and its gradient at $x/L = 0.97$ get closer to the reference data, as shown in the left column of Fig. 11. However the linearized wall model is less sensitive to this treatment as the gradient is essentially linearized and limited. It can be observed that the deviation from the linear solution of the working viscosity becomes more severe after the gradient correction in the non-linear wall model. This indicates that further protection for the near wall solution is needed.

The working viscosity along with the normal gradient is therefore enforced simultaneously in fluid interior points close to wall with their theoretical solutions. The threshold is initially set to $y_c^+ = 300$. Fig. 12 shows that skin friction is significantly improved in both wall models. Moreover the flow field profiles follow the reference values well, except for the eddy viscosity and good grid convergence has been obtained, as illustrated by Fig. 13. Different enforcement thresholds are investigated for the skin friction on the medium grid in Fig. 14. The curves are almost superposed, indicating that the near wall solution

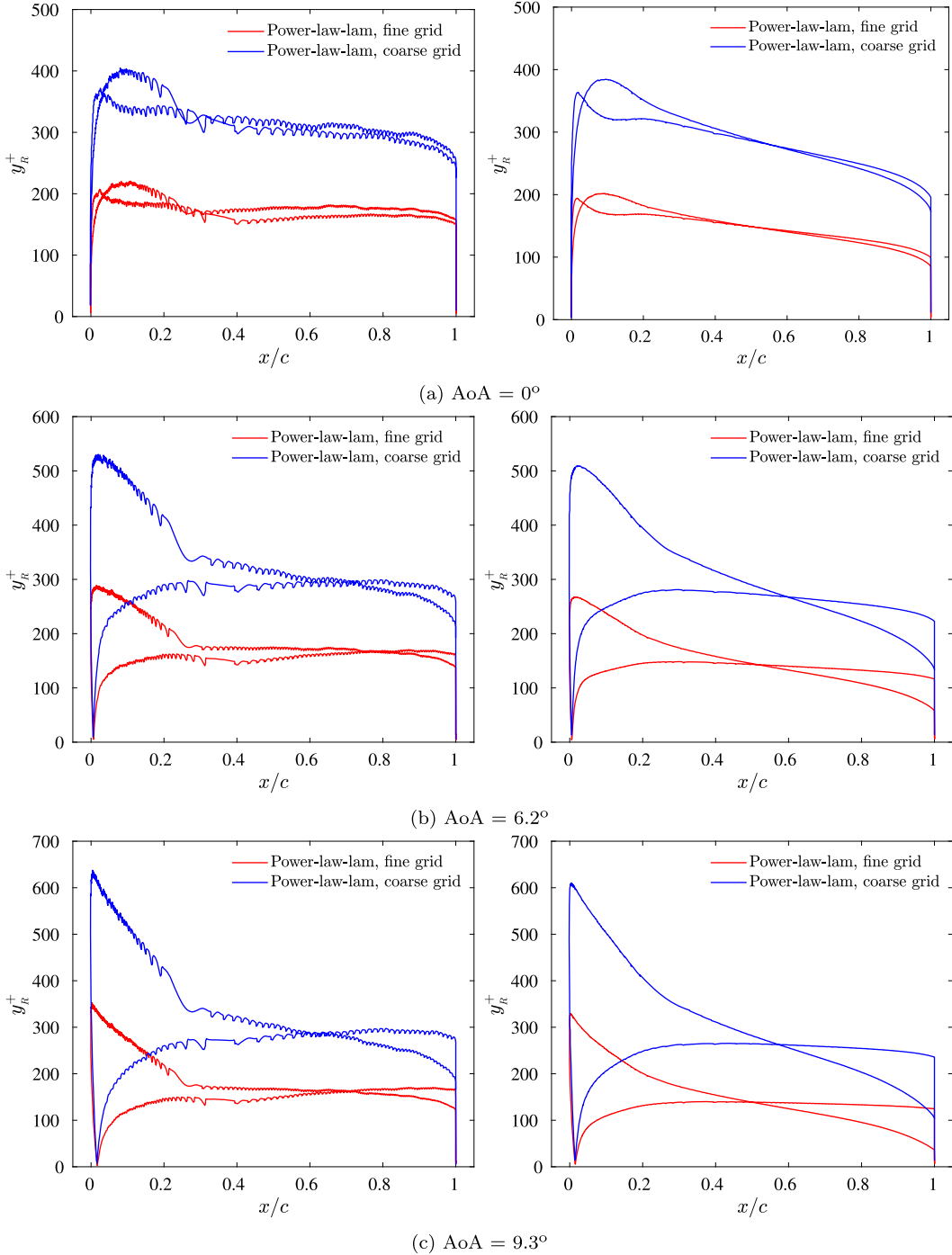


Fig. 26. Comparison of y^+ at the reference point at different AoAs for the original IBM (left) and the improved IBM (right). (For interpretation of the colors in the figure(s), the reader is referred to the web version of this article.)

is well protected when the threshold is chosen in a reasonable range. Furthermore different boundary conditions for the normal velocity are compared in Fig. 15. No substantial changes have been found toward the constant, linear and quadratic approximations.

In addition to the normal gradient correction and the near wall field enforcement, Fig. 16 shows the skin friction computed with the u_τ interpolation and the WLSQ gradient scheme using equation (57). The effect of WLSQ gradient scheme is found very small in this case. This can be explained by the fact that the gradient in the wall parallel direction is calculated by the second order centered differencing which shares the same accuracy as the WLSQ method, and the normal gradient

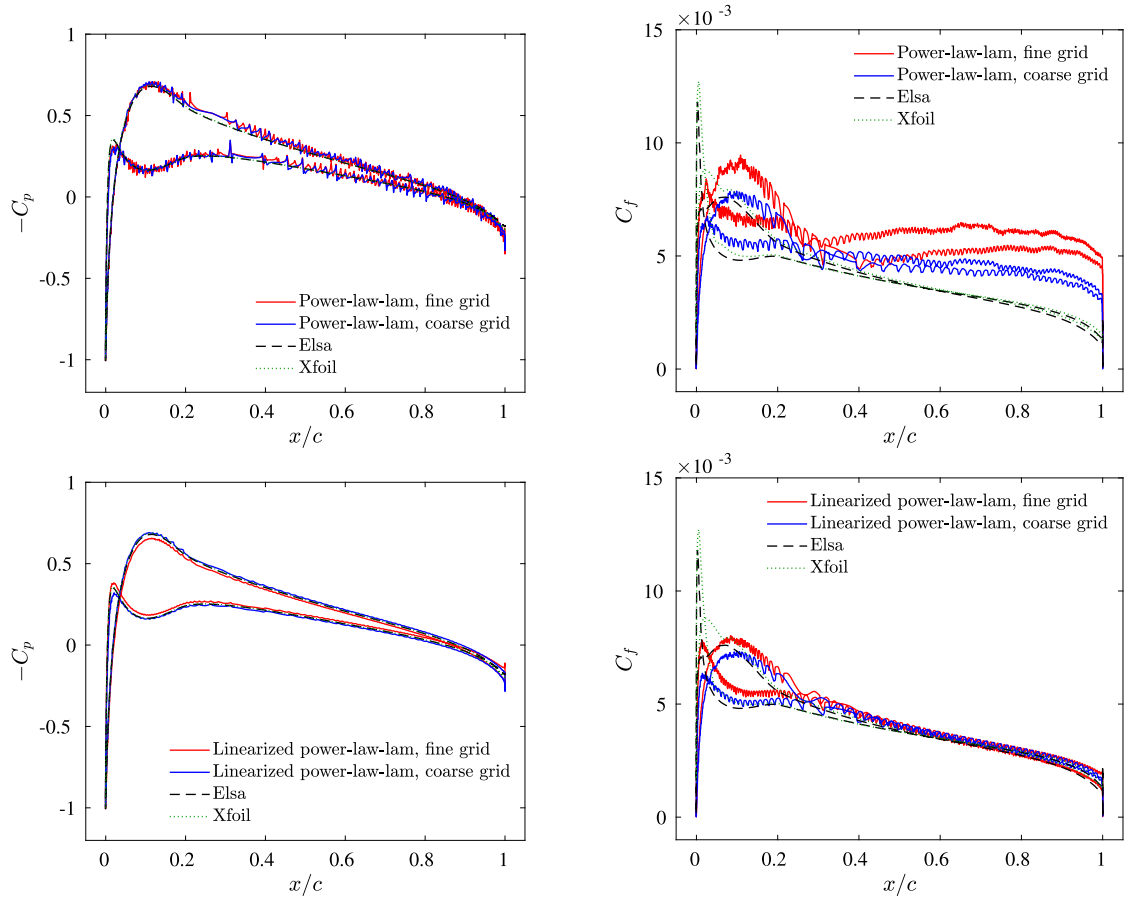


Fig. 27. Comparison of wall surface pressure and skin friction for the original IBM with the non-linear wall model and the linearized wall model at AoA = 0°. Top for non-linear wall model and bottom for linearized wall model. (For interpretation of the colors in the figure(s), the reader is referred to the web version of this article.)

is finally corrected by the law of the wall. In current test the near wall points are principally located in the logarithmic layer such that the velocity variation is not significant. Hence the interpolation for u_τ with the inverse distance weighting method does not differ too much from the interpolation for the velocity. In fact the u_τ interpolation yields a slightly higher value of the skin friction. The result almost stays the same by further applying the interpolation in the tangential direction for ρ . This comes from the fact that ρ exhibits diminishing variation in the wall normal direction, so that it is not sensitive to the treatment of interpolation. Even though it does not play an important role here, it helps to remove the need of the ambiguous reference point.

In the following, the Cartesian grid is inclined at different angles such that the IBC is applied at the stair case grid boundaries, which occurs frequently in general simulations. In this situation, it is impossible to ensure that near wall points always stay in the logarithmic layer as in the aligned grid case. The boundary points certainly cross different wall layers along the plate, yielding significant variation of the computed gradient. Fig. 17 shows the skin friction calculated by the original IBM for the non-linear and linearized wall models with large spurious oscillations. In the non-linear wall model the mean value of the skin friction deviates considerably from the reference data, while it converges under grid refinements in the linearized wall model.

Applying the normal gradient correction (61), the skin friction is dramatically reduced in the non-linear wall model, as shown in Fig. 18. The linearized wall model is essentially not affected by this correction just as in the aligned grid case because the gradient is made constant below the reference point. However enforcing the flow fields near wall does change the results for both wall models, as shown in Fig. 19. The skin friction computed on the medium grid gets close to the result on the fine grid. After the application of the WLSQ gradient scheme (57), the skin friction is significantly improved in the non-linear wall model in Fig. 20. Again the linearized wall model is insensitive to this gradient computation. But now the two wall models give very similar results. Fig. 21 shows the skin friction by activating the u_τ interpolation. Oscillations are almost removed. Clean results have been obtained in the linearized wall model but the skin friction is slightly underestimated on the fine grid. Again employing tangential interpolation for ρ shows no evident difference.

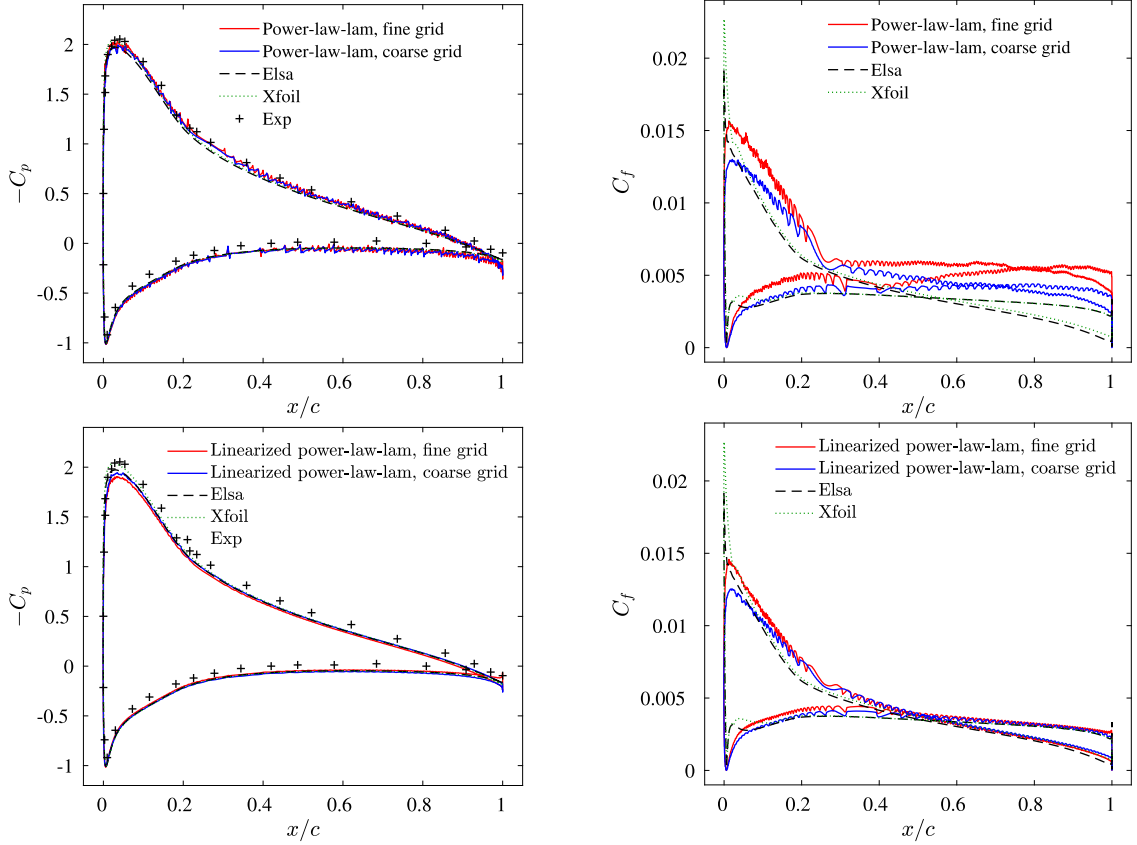


Fig. 28. Comparison of wall surface pressure and skin friction for the original IBM with the non-linear wall model and the linearized wall model at $\text{AoA} = 6.2^\circ$. Top for nonlinear wall model and bottom for linearized wall model. (For interpretation of the colors in the figure(s), the reader is referred to the web version of this article.)

The normal velocity boundary conditions are re-examined for the stair-case boundary, as shown in Fig. 22. Using higher order approximations results in a relatively higher value of the skin friction compared to Fig. 21. The influence of interpolation methods for u_τ is also investigated in Fig. 23. The IDW method is often believed to give too many weights to far away neighbor points. This can be handled by increasing the power of the inverse distance. It however shows no significant modifications to the skin friction from $p = 2$ to $p = 5$. Apart from that, the IDW method is considered to be less accurate as it can only reproduce exactly constant fields. Using high order interpolation method by WLSQ with linear or quadratic basis does not lead to any improvements in this case. Note that the IDW method is equivalent to the WLSQ method with the constant basis. Therefore, it can be concluded that the u_τ is a well behaved variable near wall such that it can be accurately interpolated even with the low order interpolation method.

Finally the grid is inclined to 45° to show that present IBM can preserve the accuracy under different orientations of the plate with respect to the Cartesian grid, as demonstrated by Fig. 24. It also compares the skin friction directly projected from the boundary points and the solution extrapolated to the surface point (see Fig. 4 for algorithm illustration). Similar results have been found and the surface extrapolation provides additional small smoothing effect towards the quantity of interest.

4.2. NACA 23012 airfoil case

For further validation with an industry-relevant geometry, the turbulent flow around a non-symmetric NACA 23012 airfoil is simulated at three angles of attack $\text{AoA} = 0^\circ, 6.2^\circ$ and 9.3° , as the experimental results from [83] are available for comparison. The Reynolds number based on the chord length c is 1.88×10^6 and the freestream Mach number is 0.18. This case was extensively studied in [50] with various Spalart-Allmaras turbulence models, including the f_{v3} variant, and the results were shown to be independent of any particular version. The size of the computational domain is chosen to be $[-30c, 60c] \times [-30c, 30c]$ where the airfoil is placed at the origin. For this 2D case, the grid surrounds a thin slice of the airfoil with periodic conditions applied at the spanwise direction. A uniform Cartesian grid is initially used to cover the computational domain and then locally refined in an octree pattern around the airfoil. Fig. 25 shows the final grid around the airfoil as well as a detailed view at the leading and trailing edges. Note that the sharp trailing edge is slightly trimmed

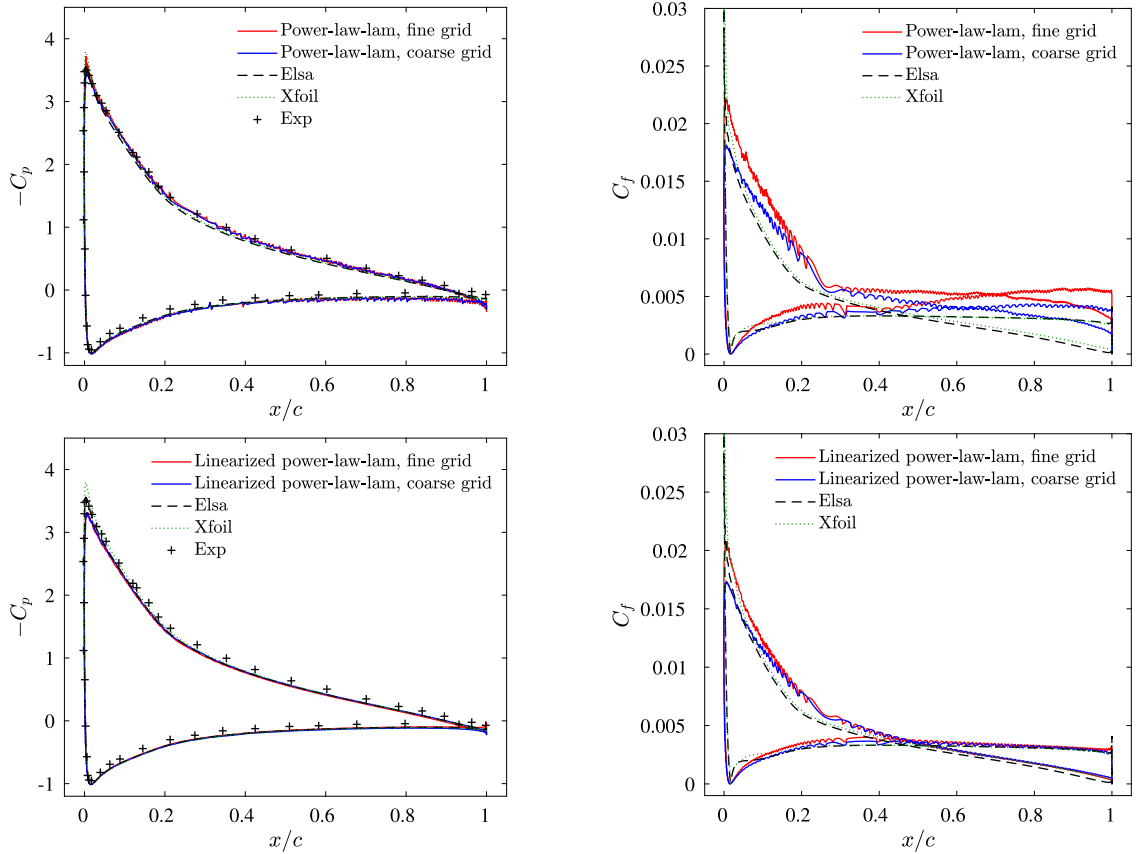


Fig. 29. Comparison of wall surface pressure and skin friction for the original IBM with the non-linear wall model and the linearized wall model at AoA = 9.3° . Top for nonlinear wall model and bottom for linearized wall model. (For interpretation of the colors in the figure(s), the reader is referred to the web version of this article.)

to avoid potential instabilities, and the overall results are essentially unchanged. Two depths of refinement are employed in current work for the grid convergence study, leading to the coarse grid with $h_{\min}/c = 1.36 \times 10^{-3}$ and the fine grid with $h_{\min}/c = 6.79 \times 10^{-4}$. The resulting y^+ at the reference point can be viewed in Fig. 26 which is mostly below 400 and 200 for the coarse grid and fine grid respectively. The inflow boundary conditions are adjusted for obtaining different angles of attack, instead of rotating the airfoil, so that the grid remains identical.

The proposed method aims at extending the applicability of the original IBM [50] to the skin friction prediction. The far field integration approach was used in [50] to determine the drag and lift coefficients. In current work the near field and far field force integration methods will be investigated simultaneously. The computed surface pressure and skin friction coefficients, as well as their integrated coefficients, will be compared to the Xfoil predictions [84] and the experimental data of [83]. In addition, the traditional body-fitted simulations are conducted as another reference data using the elsA software [85] with wall resolved grid ($y^+ < 1$ near wall).

The wall surface pressure and the skin friction computed by the original IBM with non-linear and linearized wall models are displayed in Figs. 27–29. Large wiggles are observed towards these surface quantities in the non-linear wall model. The pressure coefficient is found oscillating around the reference value, while the skin friction deviates considerably and shows an inconsistent trend from the 30% of the chord down to the trailing edge, especially on the fine grid. After the application of the linearization technique, the wall pressure is indeed smoothed for all angles of attack, which is also found in [50]. Whereas the pressure near the leading edge at the suction side gets slightly under-estimated after grid refinement. The predicted skin friction shows a good trend towards the reference value using the linearized wall model although the oscillations are still evident.

Figs. 30 and 31 compare the drag coefficient and the lift coefficient from the near field and far field integration approaches for different wall models under grid refinement. No significant difference has been found for the lift coefficient, with respect to the integration method and the grid refinement. However the non-linear wall model gives a slightly over-estimated lift coefficient at large AoA. As for the drag coefficient, it is considerably over-estimated with the near field approach in both non-linear and linearized wall models, compared to the far field approach. This is mainly due to the spurious oscillations at wall that are gradually dissipated far away. The linearized wall model yields a better near field drag coefficient as the oscillation is reduced for the wall pressure. By refining the grid, the near field and far field results move

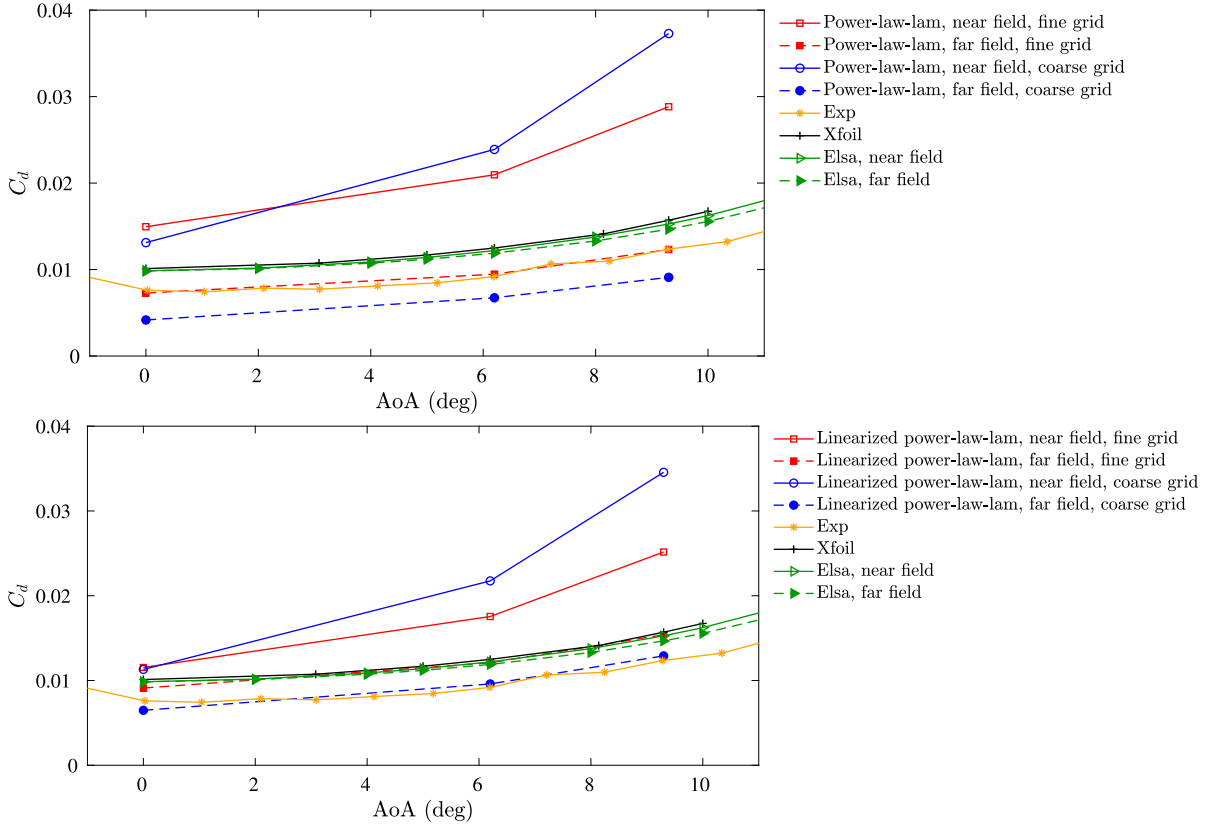


Fig. 30. Comparison of the drag coefficient for the original IBM with the non-linear wall model and the linearized wall model at different AoAs. Top for nonlinear wall model and bottom for linearized wall model. (For interpretation of the colors in the figure(s), the reader is referred to the web version of this article.)

closer to each other for both wall models. The far field drag coefficient obtained by the non-linear wall model on the fine grid falls within the range of the experimental results and the numerical reference data, while it is slightly over-estimated by the linearized wall model on the fine grid at large AoA.

Next the proposed techniques are applied to enhance the near wall solution of the non-linear wall model, namely the tangential interpolation for u_τ and ρ , the WLSQ gradient scheme (57), the reconstruction of the normal gradient by the law of the wall (61), the enforcement of eddy viscosity and normal gradient in the near wall cells. As demonstrated in the previous case, the linearized wall model is essentially not affected by the gradient calculation methods. Nevertheless it can be significantly improved by the new interpolation method and the near wall field enforcement. The results are shown in Figs. 32–34. The spurious oscillations on the wall pressure and the skin friction have been almost eliminated for both the non-linear and the linearized wall models at every AoA. Despite the skin friction being slightly over-estimated, the wall pressure is computed quite well with both wall models. It can be observed that the linearized wall model yields smoother results, but the wall pressure at the suction side near the leading edge gets under-estimated after grid refinement, which is actually influenced by the linear velocity profile enforced near the wall. This can be further verified in Fig. 35 for the comparison of different wall models at $\text{AoA} = 6.2^\circ$ on both coarse and fine grids.

In industrial applications, the computational grid has to be refined in some specific regions when high resolution is needed. To demonstrate the fidelity of current approach for handling different grid resolutions near wall boundaries, the grid is locally refined around the leading edge of the airfoil based on the coarse grid, as shown in Fig. 25. The results at $\text{AoA} = 6.2^\circ$ labeled by the transition grid in Fig. 36 reveal a slight jump across the grid transition interface, more evidently on the skin friction. This jump is essentially caused by the computation of the velocity normal gradient as it is linked to the grid resolution in equation (61). The skin friction computed on the transition grid is very close to the fine grid results in the refined region. It approaches the coarse grid results towards the trailing edge except for a slight over-estimation on the suction side. Nevertheless it has a negligible effect on the wall pressure. We also compare different treatments of the normal velocity boundary conditions and the influence is found negligible, see Fig. 37.

The integrated coefficients by the present IBM are shown in Figs. 38 and 39. With the far field integration, the drag is higher than the reference level for both models on the fine grid, but the difference to the near field estimation is greatly reduced compared to the original IBM. The proposed ingredients dramatically improve the drag prediction of the non-linear wall model with the near field integration. The linearized wall model has also received improvements at small AoAs.

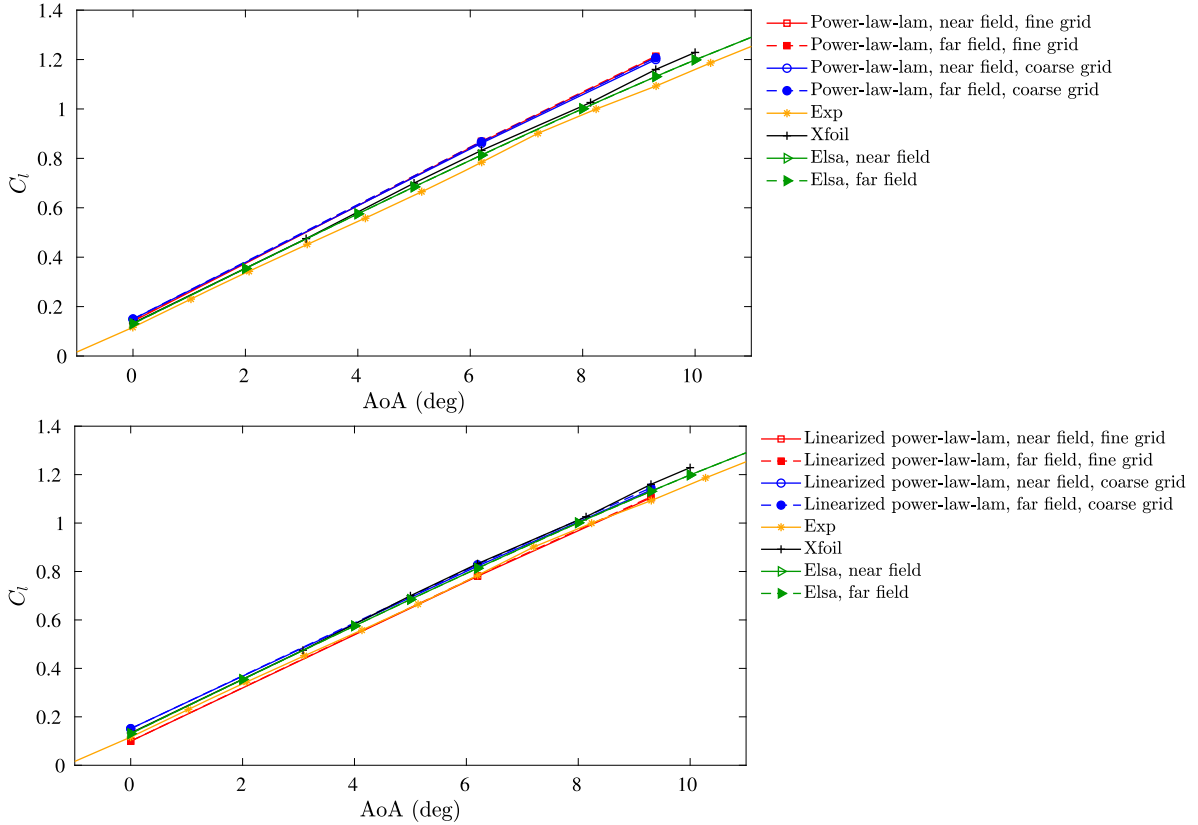


Fig. 31. Comparison of the lift coefficient for the original IBM with the non-linear wall model and the linearized wall model at different AoAs. Top for nonlinear wall model and bottom for linearized wall model. (For interpretation of the colors in the figure(s), the reader is referred to the web version of this article.)

This comes from the fact that the viscous contribution to the total drag dominates the pressure part at $\text{AoA} = 0^\circ$ and becomes comparable at $\text{AoA} = 6.2^\circ$ in this case. The reduction of oscillations of the skin friction hence improves the drag in the linearized wall model. Actually, the drag coefficient is found very close between the non-linear wall model and the linearized wall model after applying those ingredients. The proposed IBM improves the agreement between the predicted lift and the reference for the non-linear wall model, whereas there is almost no change for the linearized wall model. The predicted lift has shown to be invariant under grid refinement in the non-linear wall model, while it experiences a decrease in the linearized wall model when refining the grid. There is certainly room for further grid refinement for this case. But current results clearly show that the linearization is not necessary for obtaining smoothed surface quantities as long as the gradient is taken carefully in conjunction with the other improvements. Consequently physical wall law can be respected without any numerical adaptations and physically consistent results can be obtained.

4.3. 3D trap wing case

As our last validation case, we consider the NASA trap wing benchmark test defined in the 1st AIAA CFD High Lift Prediction Workshop [86], more precisely the configuration 1 with slat 30 and flap 25 without brackets. The Mach number is 0.2 and the Reynolds number is 4.3×10^6 based on the mean aerodynamic chord (1.0067 m). The angle of attack $\text{AoA} = 13^\circ$ is simulated by inclining the inflow velocity. The computational domain is taken as $40 \text{ m} \times 15 \text{ m} \times 30 \text{ m}$ to encompass a half wing. Symmetry boundary conditions are applied to the symmetry plane and the lateral boundary. Two different grids are compared in this study. The coarse grid consists of about 18.3 million grid points with a near wall grid resolution of 2.5 mm, while the fine grid contains around 69.6 million grid points with a finer grid spacing of 1.25 mm near the wall. Even though the grids are still marginal for the modeled turbulent boundary layer, the results are found very good with the improved IBM. Fig. 40 displays the distribution of wall pressure and skin friction over the wing surface using the non-linear wall model. The corresponding wall pressure coefficient is extracted at several locations $\eta = 0.17, 0.28, 0.41, 0.50, 0.65, 0.70, 0.85, 0.95, 0.98$ of the span, as shown in Fig. 41. The results are quite smooth and agree well with the available experimental data in [86]. The drag and lift coefficients are listed in Table 2. The far field integration domain surrounding the wing is taken to be $4.2 \text{ m} \times 2.8 \text{ m} \times 2.0 \text{ m}$ that is very close to the wing body. The overall quality

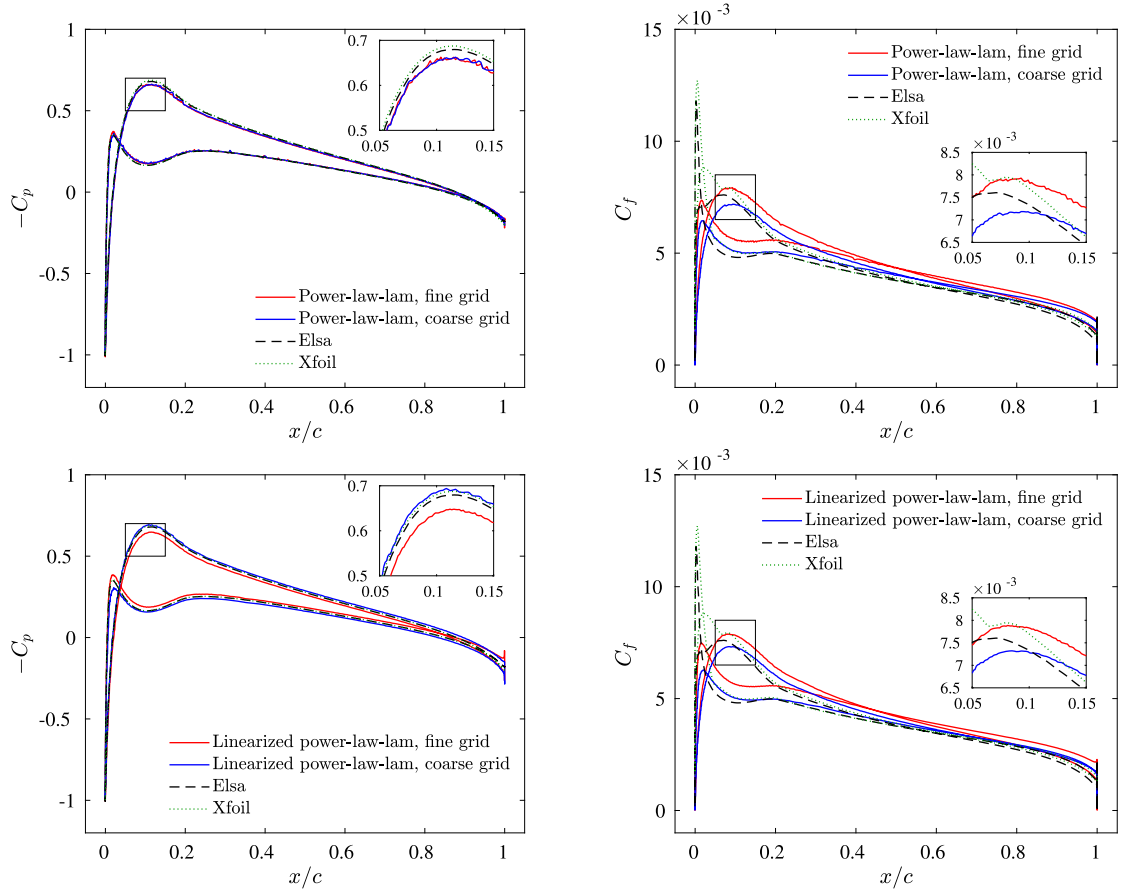


Fig. 32. Comparison of wall surface pressure and skin friction for the improved IBM with the non-linear wall model and the linearized wall model at $AoA = 0^\circ$. Top for nonlinear wall model and bottom for linearized wall model. (For interpretation of the colors in the figure(s), the reader is referred to the web version of this article.)

Table 2

Comparison of drag and lift coefficients of the NASA trap wing for the improved IBM with the non-linear wall model.

	Method	Grid	C_d	C_l
Experiment [86]	-	-	0.3330	2.0468
PowerFLOW [86]	-	Coarse, $h_{\min} = 1.5$ mm	0.3276	2.0101
PowerFLOW [86]	-	Fine, $h_{\min} = 1.25$ mm	0.3329	2.0641
PowerFLOW [86]	-	Very fine, $h_{\min} = 1.0$ mm	0.3311	2.0616
Present	Near field	Coarse, $h_{\min} = 2.5$ mm	0.3357	1.7980
Present	Far field	Coarse, $h_{\min} = 2.5$ mm	0.2906	1.7682
Present	Near field	Fine, $h_{\min} = 1.25$ mm	0.3462	1.8687
Present	Far field	Fine, $h_{\min} = 1.25$ mm	0.3123	1.8090

of the present results is satisfactory, with an accuracy similar to the one reported in [86] in other simulations based on Cartesian grids with immersed boundaries.

5. Conclusions

An improved coupling of immersed boundaries and turbulent wall models on Cartesian grids has been presented for high Reynolds number RANS flow simulations. Smooth wall surface quantities such as the wall pressure and the skin friction have been obtained with the proposed method in the presence of irregular wall distance of the computational boundary, along with more accurate integral quantities of the drag and lift coefficients. The key ingredients are the tangential interpolation for u_τ , the WLSQ gradient scheme, the reconstruction of normal gradient at the approximated boundaries, as well as the enforcement of eddy viscosity from the turbulence model in fluid close to wall.

The proposed interpolation has completely eliminated the use of the ambiguous reference point and considerably reduced the spurious oscillations in the results. It however requires the calculation of wall distance in fluid interior points

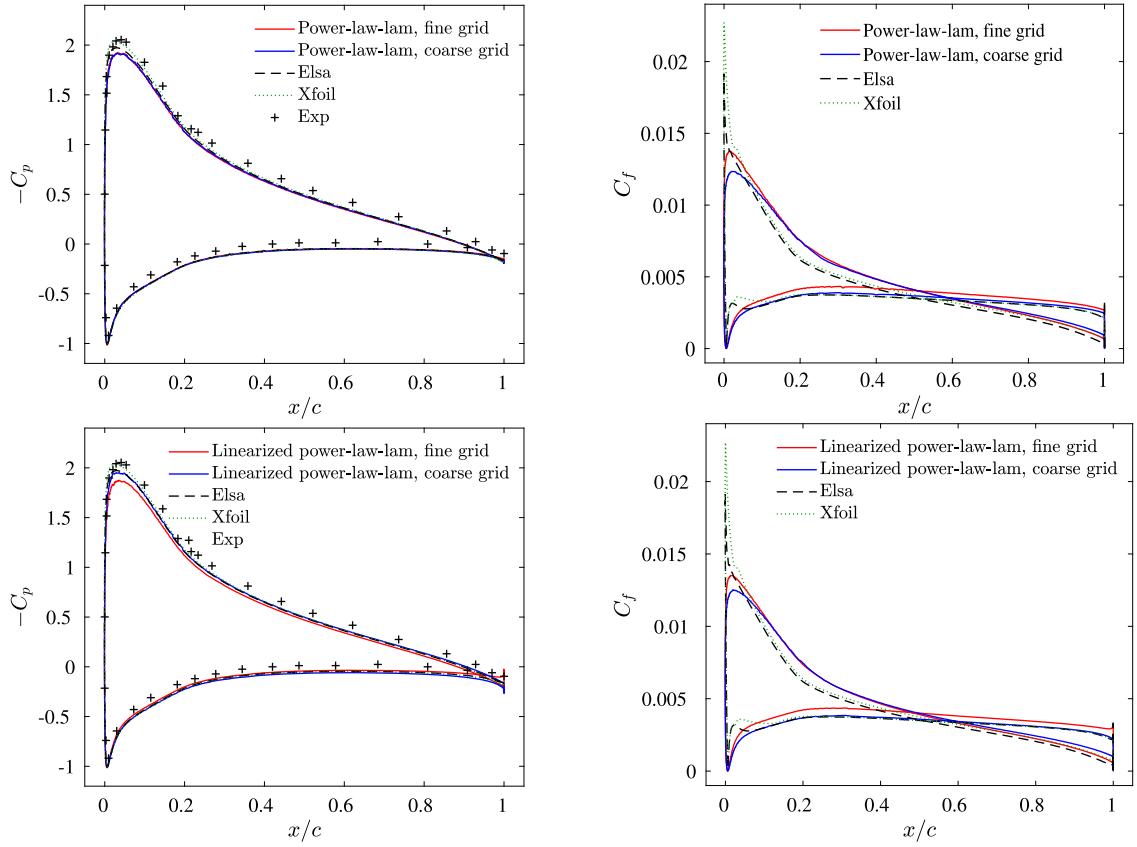


Fig. 33. Comparison of wall surface pressure and skin friction for the improved IBM with the non-linear wall model and the linearized wall model at $\text{AoA} = 6.2^\circ$. Top for nonlinear wall model and bottom for linearized wall model. (For interpretation of the colors in the figure(s), the reader is referred to the web version of this article.)

near the wall, which might be unfeasible for some wall-distance-free turbulence models other than the classical Spalart-Allmaras model. It also inverts the wall function more times than the usual approach but the computational time is not increased significantly thanks to the explicit wall model used. The current treatment of gradients has achieved the correct behavior of the skin friction in the wall function approach, which has been further enhanced by the near wall eddy viscosity distribution. In terms of efficiency, the major increase of the computational time is associated with the gradient computation, which however is often observed in other software.

The linearization of the near-wall velocity profile has been proven unnecessary in reducing the spurious oscillations in current LBM based solver, once the gradients are well handled with the non-linear velocity profile. Hence the exact law of the wall has been maintained for the physical behavior near the wall. Even though the surface quantities are produced more smoothly by linearization, the wall pressure is not well predicted under grid refinement. Other numerical aspects with respect to the interpolation's weight and order of precision, the normal velocity boundary condition and the post-processing of surface quantities have also been investigated and shown very little effect to the final results.

Although the current work is carried out in the framework of LBM simulation, the techniques developed here can be applied straightforwardly to Navier-Stokes based solvers, since all the modifications are applied to the macroscopic variables. The proposed method is very simple to implement and quite efficient for industrial applications of attached flows at high Reynolds numbers due to the use of the explicit power-law based wall function. Furthermore the present method may be further improved and extended to a wide range of problems by incorporating the effects of the buffer layer, the pressure gradient and the curvature in the wall model.

CRedit authorship contribution statement

Shang-Gui Cai: Conceptualization, Methodology, Software, Validation, Formal analysis, Writing – Original Draft. **Johan Degrigny:** Conceptualization, Methodology, Software, Writing – Reviewing and Editing. **Jean-François Bousuge:** Project administration, Supervision, Resources, Writing – Reviewing and Editing. **Pierre Sagaut:** Project administration, Supervision, Resources, Writing – Reviewing and Editing.

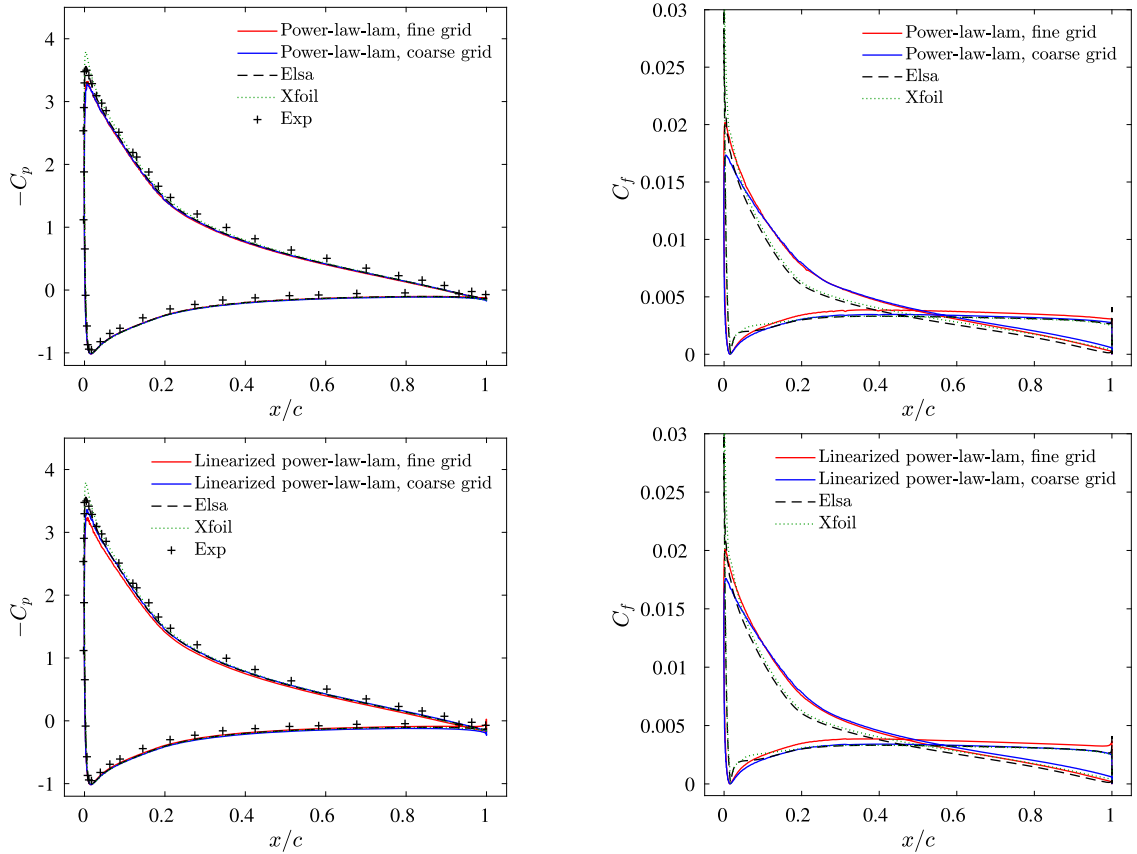


Fig. 34. Comparison of wall surface pressure and skin friction for the improved IBM with the non-linear wall model and the linearized wall model at AoA = 9.3° . Top for nonlinear wall model and bottom for linearized wall model. (For interpretation of the colors in the figure(s), the reader is referred to the web version of this article.)

Declaration of competing interest

The authors declare that they have no known competing financial interests or personal relationships that could have appeared to influence the work reported in this paper.

Acknowledgement

The Centre de Calcul Intensif d'Aix-Marseille is acknowledged for granting access to its high performance computing resources. This work was supported by DGAC project No. 2018-16 OMEGA3 and ANR Industrial Chair ALBUMS (grant ANR-18-CHIN-0003-01). The authors acknowledge valuable discussions with Jérôme Jacob and Sylvia Wilhelm.

References

- [1] G. Iaccarino, R. Verzicco, Immersed boundary technique for turbulent flow simulations, *Appl. Mech. Rev.* 56 (3) (2003) 331–347.
- [2] R. Mittal, G. Iaccarino, Immersed boundary method, *Annu. Rev. Fluid Mech.* 37 (1) (2005) 239–261.
- [3] F. Sotiropoulos, X. Yang, Immersed boundary methods for simulating fluid-structure interaction, *Prog. Aerosp. Sci.* 65 (2014) 1–21.
- [4] H. Johansen, P. Colella, A Cartesian grid embedded boundary method for Poisson's equation on irregular domains, *J. Comput. Phys.* 147 (1998) 60–85.
- [5] T. Ye, R. Mittal, H. Udaykumar, W. Shyy, An accurate Cartesian grid method for viscous incompressible flows with complex immersed boundaries, *J. Comput. Phys.* 156 (2) (1999) 209–240.
- [6] H. Udaykumar, R. Mittal, P. Rampunggoon, A. Khanna, A sharp interface Cartesian grid method for simulating flows with complex moving boundaries, *J. Comput. Phys.* 174 (1) (2001) 345–380.
- [7] R. LeVeque, Z. Li, The immersed interface method for elliptic equations with discontinuous coefficients and singular sources, *SIAM J. Numer. Anal.* 31 (1994) 1019–1044.
- [8] D. Huang, D. Santis, C. Farhat, A family of position- and orientation-independent embedded boundary methods for viscous flow and fluid-structure interaction problems, *J. Comput. Phys.* 365 (2018) 74–104.
- [9] R. Glowinski, T. Pan, J. Periaux, A fictitious domain method for external incompressible viscous flows modeled by Navier-Stokes equations, *Comput. Methods Appl. Mech. Eng.* 112 (1994) 133–148.
- [10] R. Löhner, Towards overcoming the LES crisis, *Int. J. Comput. Fluid Dyn.* 33 (3) (2019) 87–97.
- [11] C.S. Peskin, Flow patterns around heart valves: a numerical method, *J. Comput. Phys.* 10 (2) (1972) 252–271.

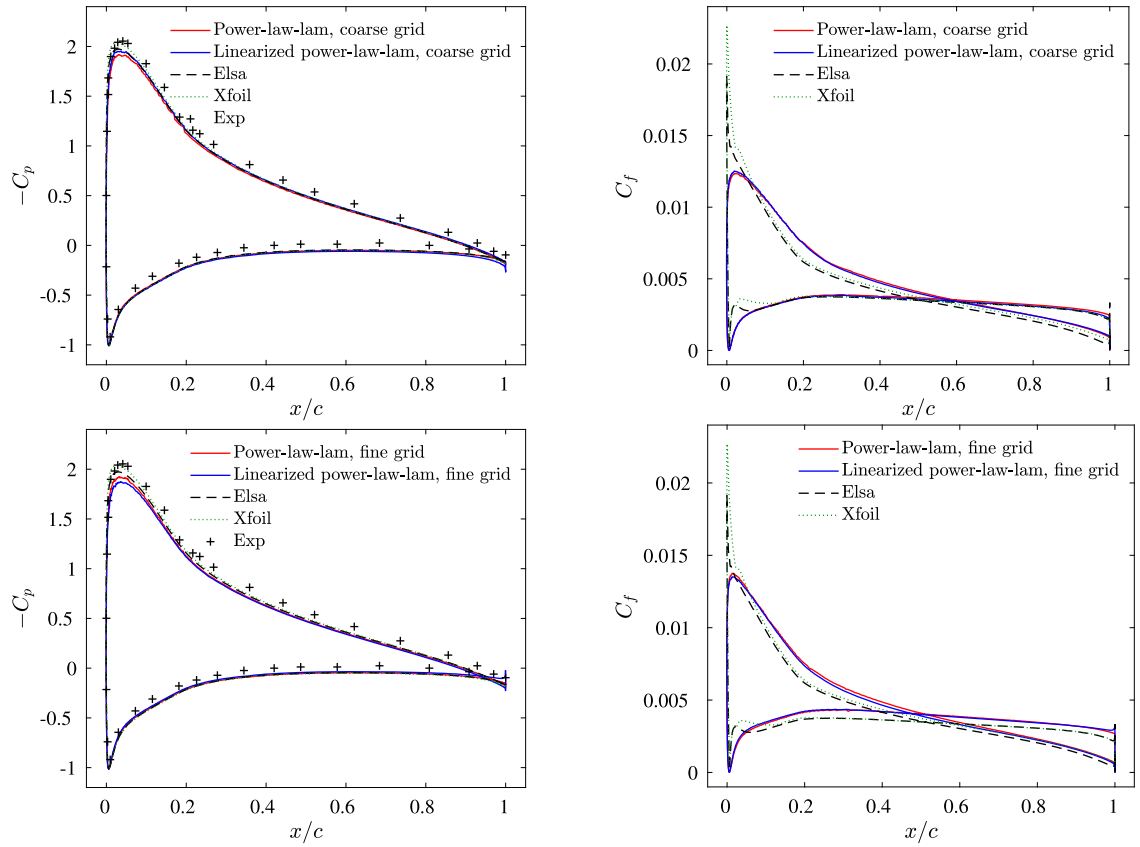


Fig. 35. Comparison of nonlinear and linearized wall models for the improved IBM at $\text{AoA} = 6.2^\circ$. (For interpretation of the colors in the figure(s), the reader is referred to the web version of this article.)

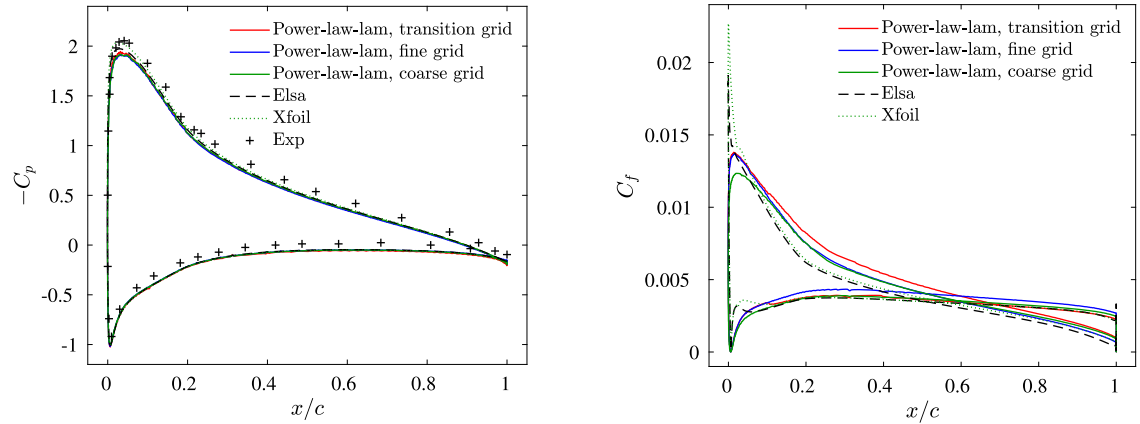


Fig. 36. Comparison of grid refinement for the improved IBM with the non-linear wall model at $\text{AoA} = 6.2^\circ$. Top for the coarse grid and bottom for the fine grid. (For interpretation of the colors in the figure(s), the reader is referred to the web version of this article.)

- [12] C.S. Peskin, The immersed boundary method, *Acta Numer.* 11 (2002) 479–517.
- [13] X. Wang, W.K. Liu, Extended immersed boundary method using FEM and RKPM, *Comput. Methods Appl. Mech. Eng.* 193 (2004) 1305–1321.
- [14] L. Zhang, A. Gerstenberger, X. Wang, W.K. Liu, Immersed finite element method, *Comput. Methods Appl. Mech. Eng.* 193 (2004) 2051–2067.
- [15] B. Griffith, N. Patankar, Immersed methods for fluid–structure interaction, *Annu. Rev. Fluid Mech.* 52 (2020) 421–448.
- [16] M.-C. Lai, C. Peskin, An immersed boundary method with formal second-order accuracy and reduced numerical viscosity, *J. Comput. Phys.* 160 (2) (2000) 705–719.
- [17] D. Goldstein, R. Handler, L. Sirovich, Modeling a no-slip flow boundary with an external force field, *J. Comput. Phys.* 105 (2) (1993) 354–366.
- [18] P. Angot, C. Bruneau, A penalization method to take into account obstacles in viscous flows, *Numer. Math.* 81 (1999) 497–520.
- [19] M. Uhlmann, An immersed boundary method with direct forcing for the simulation of particulate flows, *J. Comput. Phys.* 209 (2) (2005) 448–476.

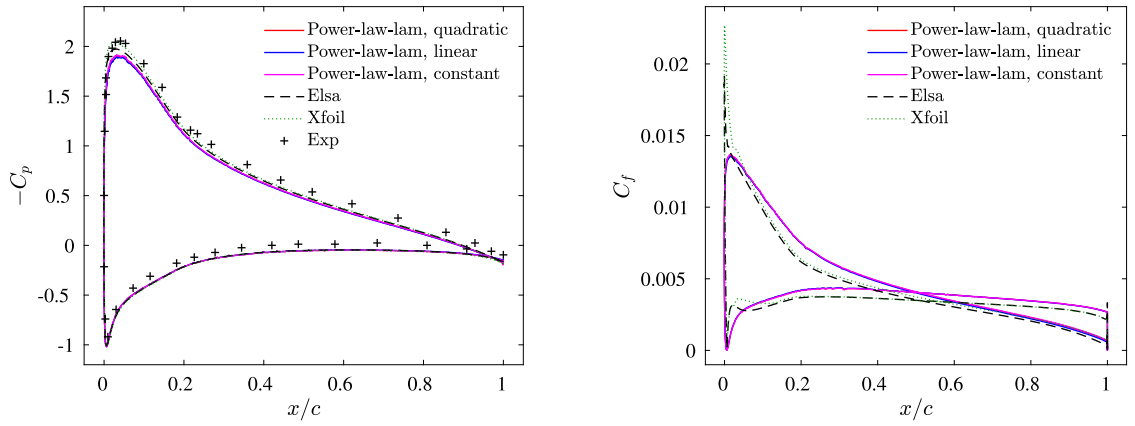


Fig. 37. Comparison of normal velocity boundary condition for the improved IBM with the non-linear wall model at $\text{AoA} = 6.2^\circ$ on the fine grid. (For interpretation of the colors in the figure(s), the reader is referred to the web version of this article.)

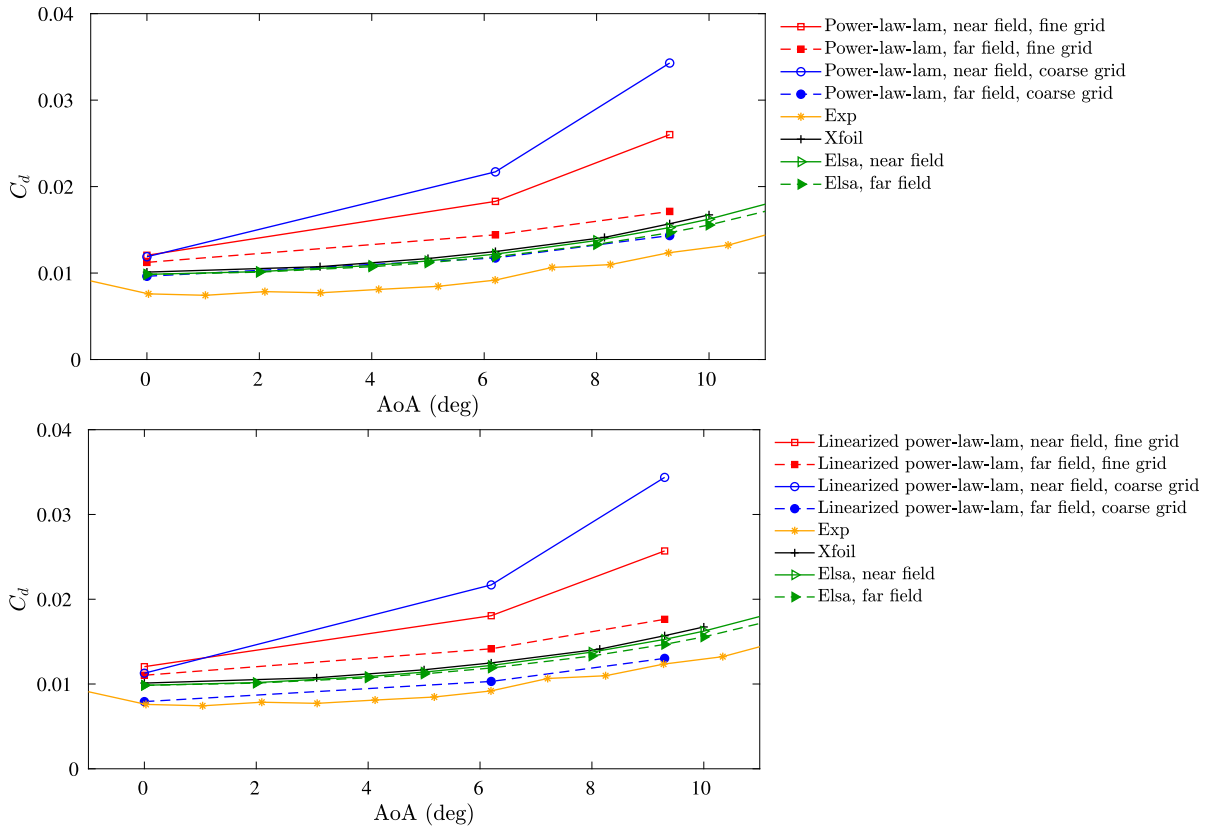


Fig. 38. Comparison of the drag coefficient for the improved IBM with the non-linear wall model and the linearized wall model at different AoAs. Top for nonlinear wall model and bottom for linearized wall model. (For interpretation of the colors in the figure(s), the reader is referred to the web version of this article.)

[20] T. Kempe, J. Fröhlich, An improved immersed boundary method with direct forcing for the simulation of particle laden flows, *J. Comput. Phys.* 231 (9) (2012) 3663–3684.

[21] K. Taira, T. Colonius, The immersed boundary method: a projection approach, *J. Comput. Phys.* 225 (2) (2007) 2118–2137.

[22] S.-G. Cai, A. Ouahsine, J. Favier, Y. Hoarau, Improved implicit immersed boundary method via operator splitting, in: A. Ibrahimbegovic (Ed.), *Computational Methods for Solids and Fluids*, vol. 41, Springer Verlag, 2016, pp. 49–66, Ch. 3.

[23] S.-G. Cai, A. Ouahsine, J. Favier, Y. Hoarau, Moving immersed boundary method, *Int. J. Numer. Methods Fluids* 85 (2017) 288–323.

[24] Y.-H. Tseng, J. Ferziger, A ghost-cell immersed boundary method for flow in complex geometry, *J. Comput. Phys.* 192 (2003) 593–623.

[25] R. Mittal, H. Dong, M. Bozkurttas, F. Najjar, A. Vargas, A. von Loebbecke, A versatile sharp interface immersed boundary method for incompressible flows with complex boundaries, *J. Comput. Phys.* 227 (10) (2008) 4825–4852.

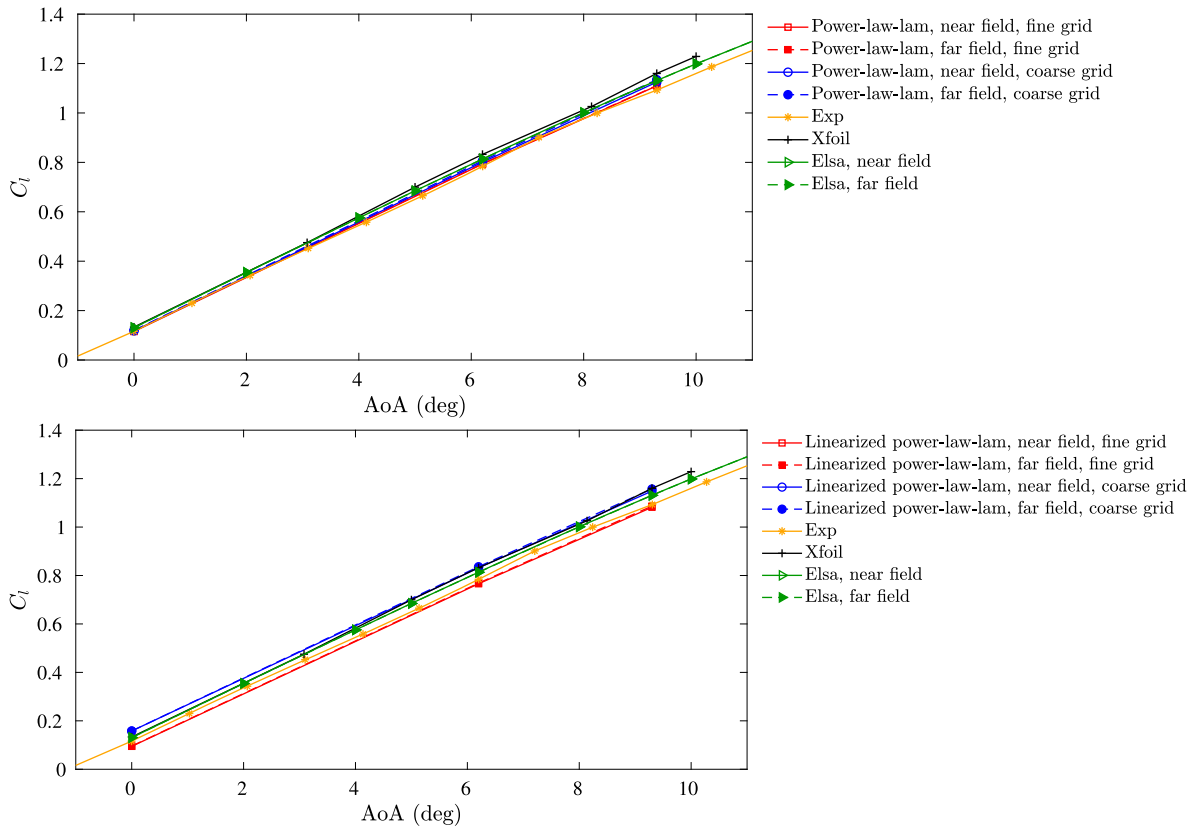


Fig. 39. Comparison of the lift coefficient for the improved IBM with the non-linear wall model and the linearized wall model at different AoAs. Top for nonlinear wall model and bottom for linearized wall model. (For interpretation of the colors in the figure(s), the reader is referred to the web version of this article.)

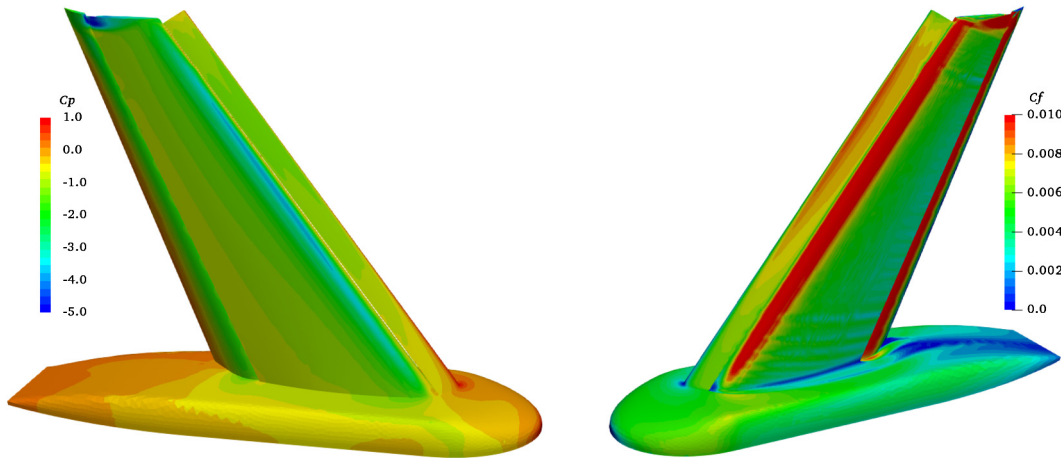


Fig. 40. Wall pressure (left) and skin friction (right) coefficients over the wing surface for the improved IBM with the non-linear wall model. (For interpretation of the colors in the figure(s), the reader is referred to the web version of this article.)

[26] M. Berger, M. Aftosmis, Progress towards a Cartesian cut-cell method for viscous compressible flow, in: 50th AIAA Aerospace Sciences Meeting Including the New Horizons Forum and Aerospace Exposition, AIAA, Nashville, 2012, pp. AIAA 2012-1301.

[27] Y. Cheny, O. Botella, The LS-STAG method: a new immersed boundary/level- set method for the computation of incompressible viscous flows in complex moving geometries with good conservation properties, J. Comput. Phys. 229 (2010) 1043-1076.

[28] X. Yang, X. Zhang, Z. Li, G.-W. He, A smoothing technique for discrete delta functions with application to immersed boundary method in moving boundary simulations, J. Comput. Phys. 228 (20) (2009) 7821-7836.

[29] A. Goza, S. Liska, B. Morley Colonius, Accurate computation of surface stresses and forces with immersed boundary methods, J. Comput. Phys. 321 (2016) 860-873.

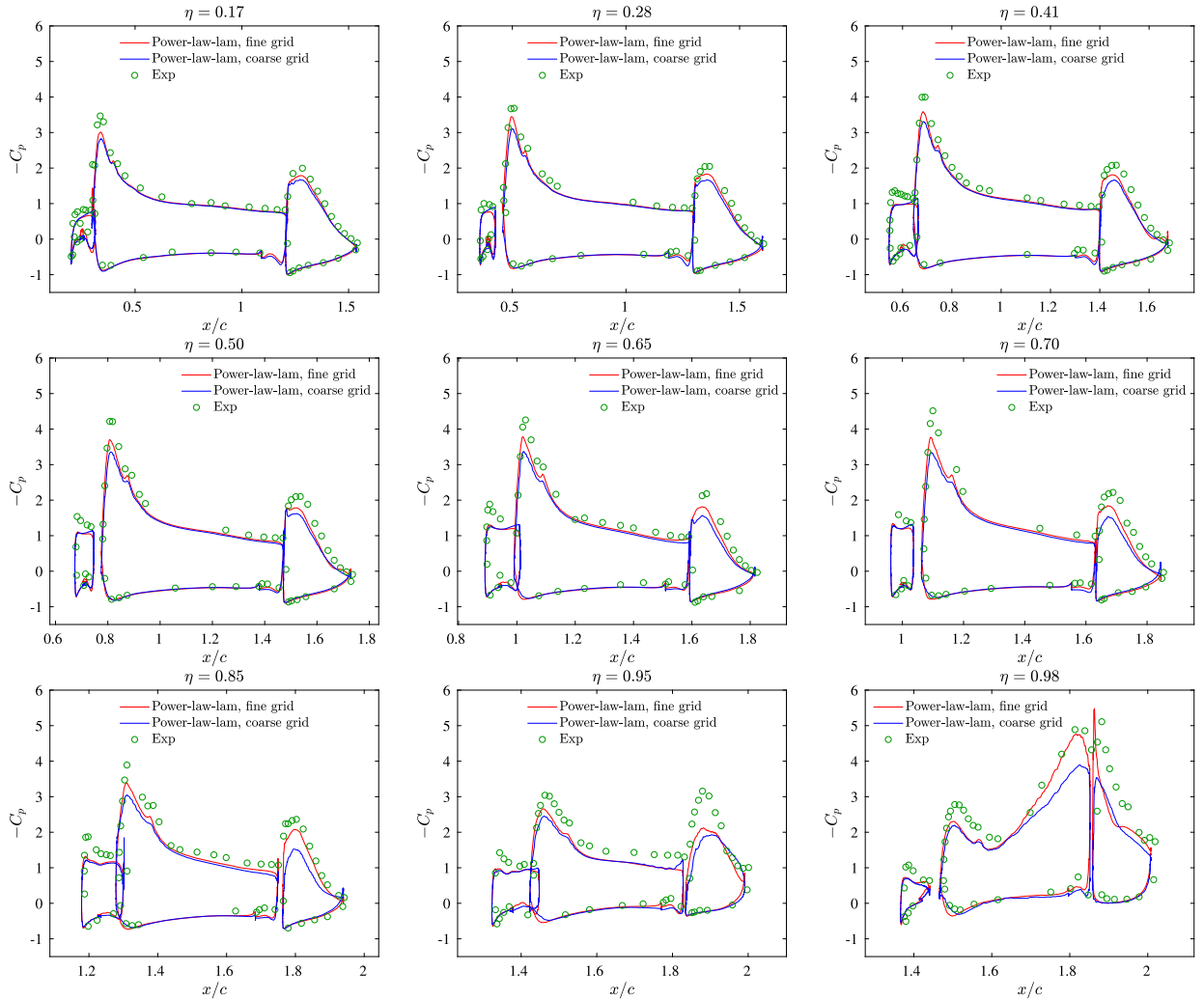


Fig. 41. Wall pressure coefficient of the 3D trap wing at different spanwise locations for the improved IBM with the non-linear wall model. (For interpretation of the colors in the figure(s), the reader is referred to the web version of this article.)

- [30] J. Mohd-Yusuf, Combined immersed boundary/B-spline methods for simulation of flow in complex geometries, *Annu. Res. Briefs, Cent. Turbul. Res.* (1997).
- [31] E. Fadlun, R. Verzicco, P. Orlandi, J. Mohd-Yusuf, Combined immersed-boundary finite-difference methods for three-dimensional complex flow simulations, *J. Comput. Phys.* 161 (1) (2000) 35–60.
- [32] S. Kang, G. Iaccarino, F. Ham, P. Moin, Prediction of wall-pressure fluctuation in turbulent flows with an immersed boundary method, *J. Comput. Phys.* 228 (2009) 6753–6772.
- [33] S. Majumdar, G. Iaccarino, P. Durbin, RANS solvers with adaptive structured boundary non-conforming grids, *Annu. Res. Briefs, Cent. Turbul. Res.* (2001).
- [34] G. Kalitzin, G. Iaccarino, Toward immersed boundary simulation of high Reynolds number flows, *Annu. Res. Briefs, Cent. Turbul. Res.* (2003).
- [35] J.-I. Choi, R. Oberoi, J. Edwards, J. Rosati, An immersed boundary method for complex incompressible flows, *J. Comput. Phys.* 224 (2007) 757–784.
- [36] M. Harada, Y. Tamaki, Y. Takahashi, T. Imamura, A novel simple cut-cell method for robust flow simulation on Cartesian grids, in: 54th AIAA Aerospace Sciences Meeting, AIAA 2016-0601, 2016.
- [37] M. Harada, Y. Tamaki, Y. Takahashi, T. Imamura, Simple and robust cut-cell method for high-Reynolds-number-flow simulation on Cartesian grids, *AIAA J.* 55 (8) (2017) 2833–2841.
- [38] F. Roman, V. Armenio, J. Frohlich, A simple wall-layer model for large eddy simulation with immersed boundary method, *Phys. Fluids* 21 (2009) 101701.
- [39] G. Kalitzin, G. Iaccarino, Turbulence modeling in an immersed-boundary RANS method, *Annu. Res. Briefs, Cent. Turbul. Res.* (2002).
- [40] M. Bernardini, D. Modesti, S. Pirozzoli, On the suitability of the immersed boundary method for the simulation of high-Reynolds number separated turbulent flows, *Comput. Fluids* 130 (2016) 84–93.
- [41] C. Zhou, RANS simulation of high-Re turbulent flows using an immersed boundary method in conjunction with wall modeling, *Comput. Fluids* 143 (2017) 73–89.
- [42] T. Pu, C. Zhou, An immersed boundary/wall modeling method for the RANS simulation of compressible turbulent flows, *Int. J. Numer. Methods Fluids* 878 (2017) 217–238.
- [43] F. Capizzano, Turbulent wall model for immersed boundary methods, *AIAA J.* 49 (11) (2011) 2367–2381.
- [44] Y. Tamaki, M. Harada, T. Imamura, Near-wall modification of Spalart-Allmaras turbulence model for immersed boundary method, *AIAA J.* (2017) 1–13.
- [45] J. Latt, B. Chopard, Lattice Boltzmann method with regularized pre-collision distribution functions, *Math. Comput. Simul.* 72 (2006) 165–168.
- [46] O. Malaspinas, Increasing stability and accuracy of the lattice Boltzmann scheme: recursivity and regularization, arXiv:1505.06900v1, 2015.

- [47] J. Jacob, O. Malaspinas, P. Sagaut, A new hybrid recursive regularised Bhatnagar-Gross-Krook collision model for lattice Boltzmann method-based large eddy simulation, *J. Turbul.* 19 (2018) 1–26.
- [48] Y. Feng, P. Boivin, J. Jacob, P. Sagaut, Hybrid recursive regularized lattice Boltzmann simulation of humid air with applications to meteorological flows, *Phys. Rev. E* 100 (2019) 023304.
- [49] Y. Feng, P. Boivin, J. Jacob, P. Sagaut, Hybrid recursive regularized thermal lattice Boltzmann model for high subsonic compressible flows, *J. Comput. Phys.* 394 (2019) 82–89.
- [50] S. Wilhelm, J. Jacob, P. Sagaut, An explicit power-law-based wall model for lattice Boltzmann method-Reynolds-averaged numerical simulations of the flow around airfoils, *Phys. Fluids* 30 (2018) 065111.
- [51] J. Latt, B. Chopard, Straight velocity boundaries in the lattice Boltzmann method, *Phys. Rev. E* 77 (2008) 056703.
- [52] J.C. Verschaeve, B. Müller, A curved no-slip boundary condition for the lattice Boltzmann method, *J. Comput. Phys.* 229 (2010) 6781–6803.
- [53] Y. Feng, S. Guo, J. Jacob, P. Sagaut, Solid wall and open boundary conditions in hybrid recursive regularized lattice Boltzmann method for compressible flows, *Phys. Fluids* 31 (2019) 126103.
- [54] H. Xu, P. Sagaut, Analysis of the absorbing layers for the weakly-compressible lattice Boltzmann methods, *J. Comput. Phys.* 245 (2013) 14–42.
- [55] S. Deck, P. Duveau, P. d’Espiney, P. Guillen, Development and application of Spalart-Allmaras one equation turbulence model to three-dimensional supersonic complex configurations, *Aerosp. Sci. Technol.* 6 (3) (2002) 171–183.
- [56] C. Rumsey, D. Allison, R. Biedron, P. Buning, CFD sensitivity analysis of a modern civil transport near buffet-onset conditions, Tech. Rep. TM-2001-211263, NASA, 2001.
- [57] C. Rumsey, B. Smith, G. Huang, Description of a website resource for turbulence model verification and validation, in: 40th AIAA Fluid Dynamics Conference and Exhibit, 2010, see also <https://turbmodels.larc.nasa.gov>, pp. AIAA-2010-4742.
- [58] S.R. Allmaras, F.T. Johnson, P.R. Spalart, Modifications and clarifications for the implementation of the Spalart-Allmaras turbulence model, in: 7th International Conference on Computational Fluid Dynamics, ICCFD7-1902, 2012.
- [59] P.R. Spalart, S. Allmaras, A one-equation turbulence model for aerodynamic flows, in: 30th Aerospace Sciences Meeting & Exhibit, 1992, AIAA-92-0439.
- [60] G. Kalitzin, G. Medic, G. Iaccarino, P. Durbin, Near-wall behavior of RANS turbulence models and implications for wall functions, *J. Comput. Phys.* 204 (2005) 265–291.
- [61] S. Deck, N. Renard, R. Laroche, P. Sagaut, Zonal detached eddy simulation (ZDES) of a spatially developing flat plate turbulent boundary layer over the Reynolds number range $3150 \leq Re_\theta \leq 14000$, *Phys. Fluids* 26 (2014) 025116.
- [62] T. Knopp, T. Alrutz, D. Schwaborn, A grid and flow adaptive wall-function method for RANS turbulence modelling, *J. Comput. Phys.* 220 (2006) 19–40.
- [63] H. Reichardt, Vollständige Darstellung der turbulenten Geschwindigkeitsverteilung in glatten Leitungen, *Z. Angew. Math. Mech.* 31 (7) (1951) 208–219.
- [64] A.J. Musker, Explicit expression for the smooth wall velocity distribution in a turbulent boundary layer, *AIAA J.* 17 (6) (1979) 655–657.
- [65] D.B. Spalding, A single formula for the law of the wall, *J. Appl. Mech.* 28 (3) (1961) 455–458.
- [66] S. Wilhelm, J. Jacob, P. Sagaut, A new explicit algebraic wall model for LES of turbulent flows under adverse pressure gradient, *Flow Turbul. Combust.* (2020), <https://doi.org/10.1007/s10494-020-00181-7>.
- [67] F. Tessicini, G. Iaccarino, M. Fatica, M. Wang, R. Verzicco, Wall modeling for large-eddy simulation using an immersed boundary method, *Annu. Res. Briefs, Cent. Turbul. Res.* (2002).
- [68] S. Kang, An improved near-wall modeling for large-eddy simulation using immersed boundary methods, *Int. J. Numer. Methods Fluids* 78 (2) (2015) 76–88.
- [69] S. Péron, C. Benoit, T. Renaud, I. Mary, An immersed boundary method on Cartesian adaptive grids for the simulation of compressible flows around arbitrary geometries, *Eng. Comput.* (2020).
- [70] D. Shepard, A two-dimensional interpolation function for irregularly-spaced data, in: Proceedings of the 23rd ACM National Conference, ACM Press, New York, 1968, pp. 517–524.
- [71] F. Capizzano, A compressible flow simulation system based on Cartesian grids with anisotropic refinements, in: 45th Aerospace Sciences Meeting and Exhibit, 2007, AIAA-2007-1450.
- [72] R. Franke, Scattered data interpolation: tests of some methods, *Math. Comput.* 38 (1982) 181–200.
- [73] G. Liu, *Meshfree Methods: Moving Beyond the Finite Element Method*, 2nd edition, CRC Press, 2009.
- [74] V. Nguyen, T. Rabczuk, S. Bordas, M. Duflo, Meshless methods: a review and computer implementation aspects, *Math. Comput. Simul.* 79 (2008) 763–813.
- [75] M. Vanella, E. Balaras, A moving-least-squares reconstruction for embedded-boundary formulations, *J. Comput. Phys.* 228 (18) (2009) 6617–6628.
- [76] A. Pinelli, I. Naqavi, U. Piomelli, J. Favier, Immersed-boundary methods for general finite-difference and finite-volume Navier–Stokes, *J. Comput. Phys.* 229 (24) (2010) 9073–9091.
- [77] F. Toja-Silva, J. Favier, A. Pinelli, Radial basis function (RBF)-based interpolation and spreading for the immersed boundary method, *Comput. Fluids* 105 (2014) 66–75.
- [78] D. Mavriplis, Revisiting the least-squares procedure for gradient reconstruction on unstructured meshes, in: 16th AIAA Computational Fluid Dynamics Conference, AIAA 2003-3986, 2003.
- [79] J. Bredberg, On the wall boundary condition for turbulence models, Internal report 00/4, Chalmers University of Technology, 2000.
- [80] C. van Dam, Recent experience with different methods of drag prediction, *Prog. Aerosp. Sci.* 35 (1999) 751–798.
- [81] L. Paparone, R. Tognaccini, Computational fluid dynamics-based drag prediction and decomposition, *AIAA J.* 41 (9) (2003) 1647–1657.
- [82] Y. Tamaki, T. Imamura, Turbulent flow simulations of the common research model using immersed boundary method, *AIAA J.* (2018) 2271–2282.
- [83] A.P. Broeren, A.J.H. E., S. Lee, M.C. Monastero, Validation of 3-D ice accretion measurement methodology for experimental aerodynamic simulation, in: 6th AIAA Atmospheric and Space Environments Conference, Atlanta, 2014, pp. AIAA 2014-2614.
- [84] M. Drela, H. Youngren, XFOIL 6.94 User Guide, 2001.
- [85] L. Cambier, S. Heib, S. Plot, The onera elsA CFD software: input from research and feedback from industry, *Mech. Ind.* 14 (3) (2013) 159–174.
- [86] C.L. Rumsey, J.P. Slotnick, M. Long, R.A. Stuever, T.R. Wayman, Summary of the first AIAA CFD high-lift prediction workshop, *J. Aircr.* 48 (2011) 2068–2079, see also <https://hiliftpw.larc.nasa.gov/index-workshop1.html>.